nature chemical biology

Article

https://doi.org/10.1038/s41589-023-01525-w

Structural basis of Cfr-mediated antimicrobial resistance and mechanisms to evade it

Received: 7 February 2023

Accepted: 11 December 2023

Published online: 18 January 2024

Check for updates

Elena V. Aleksandrova[1,8], Kelvin J. Y. Wu[2,8], Ben I. C. Tresco[2,8], Egor A. Syroegin[1], Erin E. Killeavy[3], Samson M. Balasanyants[1], Maxim S. Svetlov[4,5], Steven T. Gregory[3], Gemma C. Atkinson[6,7], Andrew G. Myers[2] ✉ & Yury S. Polikanov[1,4,5] ✉

The bacterial ribosome is an essential drug target as many clinically important antibiotics bind and inhibit its functional centers. The catalytic peptidyl transferase center (PTC) is targeted by the broadest array of inhibitors belonging to several chemical classes. One of the most abundant and clinically prevalent resistance mechanisms to PTC-acting drugs in Gram-positive bacteria is C8-methylation of the universally conserved A2503 nucleobase by Cfr methylase in 23S ribosomal RNA. Despite its clinical importance, a sufficient understanding of the molecular mechanisms underlying Cfr-mediated resistance is currently lacking. Here, we report a set of high-resolution structures of the Cfr-modified 70S ribosome containing aminoacyl- and peptidyl-transfer RNAs. These structures reveal an allosteric rearrangement of nucleotide A2062 upon Cfr-mediated methylation of A2503 that likely contributes to the reduced potency of some PTC inhibitors. Additionally, we provide the structural bases behind two distinct mechanisms of engaging the Cfr-methylated ribosome by the antibiotics iboxamycin and tylosin.

Many antibiotics employed clinically for the treatment of human infectious diseases target the bacterial ribosome and inhibit bacterial protein synthesis[1–3]. Among these, entire classes of chemically distinct antibiotics bind in or near the PTC, located within the large subunit of the bacterial ribosome, and often inhibit protein synthesis by direct competition with the binding of aminoacyl-transfer RNA (aa-tRNA) substrates. As a natural evolutionary response to antibiotic therapy, numerous antibiotic-resistance genes have emerged in pathogenic bacteria. Among the more consequential and widespread of these genes is *cfr* (chloramphenicol-florfenicol resistance), which is most widespread in Gram-positive pathogens but has also been identified in Gram-negative bacteria, including *Escherichia coli*[4,5]. The product of this gene—Cfr—is a methylase that modifies the universally conserved ribosomal adenosyl residue A2503 of the 23S ribosomal RNA by *C*-methylation at position 8 (Fig. 1a)[6,7]. This modification lies within the heart of the ribosome, near the A-site of the PTC, and confers resistance to a wide range of PTC-targeting antibiotics, including phenicols, lincosamides, oxazolidinones, pleuromutilins and streptogramins A (collectively known as $PhLOPS_A$), as well as hygromycin A and 16-membered macrolides (16MMs), which bind in the nascent peptide exit tunnel

[1]Department of Biological Sciences, University of Illinois at Chicago, Chicago, IL, USA. [2]Department of Chemistry and Chemical Biology, Harvard University, Cambridge, MA, USA. [3]Department of Cell and Molecular Biology, University of Rhode Island, Kingston, RI, USA. [4]Department of Pharmaceutical Sciences, University of Illinois at Chicago, Chicago, IL, USA. [5]Center for Biomolecular Sciences, University of Illinois at Chicago, Chicago, IL, USA. [6]Department of Experimental Medicine, Lund University, Lund, Sweden. [7]Department of Molecular Biology, Umeå University, Umeå, Sweden. [8]These authors contributed equally: Elena V. Aleksandrova, Kelvin J. Y. Wu, Ben I. C. Tresco. ✉e-mail: myers@chemistry.harvard.edu; yuryp@uic.edu

https://doi.org/10.1038/s41589-023-01525-w

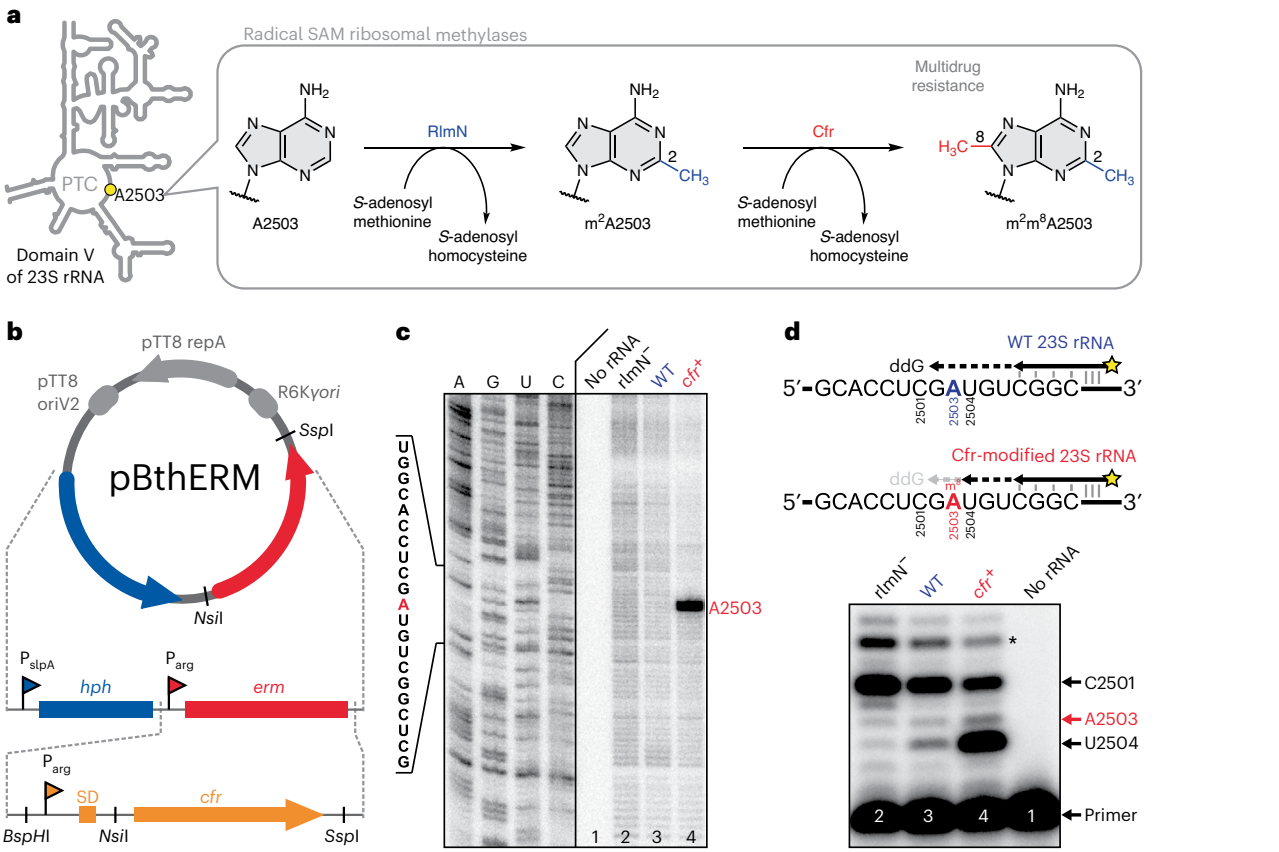

Fig. 1 | *T. thermophilus* HB27 strain expressing Cfr-like methylase. a, While nucleotide A2503 in domain V of the 23S rRNA is constitutively methylated at position C2 by the housekeeping RlmN methylase in most bacteria, C8-methylation of the same residue by Cfr-class methylases in some bacterial species results in high-level resistance to several chemically unrelated classes of PTC-targeting antibiotics. **b**, Schematic maps of the previous pBGAA1-BthERM vector (top) and its new derivatives with the *erm* gene (red) replaced by one of the six selected *cfr*-like genes (bottom) from moderately thermophilic bacteria. These vectors were designed to express Cfr methylases in *T. thermophilus* (*Tth*) HB27 cells and carry the HygB resistance marker *hph* under the control of P_{slpA} promoter (blue) and a *cfr*-like gene under the control of P_{arg} promoter (orange). **c**, Primer extension analysis of 23S rRNA isolated from *cfr*$^+$ *Tth* cells transformed with pBGAA1-PfuCFR vector (*cfr*$^+$) and control (*cfr*$^-$) WT *Tth* cells. 23S rRNA isolated from the *Tth* HB27 *rlmN*$^-$ strain lacking A2503-C2-methylation was used as an additional negative control. Sequencing lanes are shown on the left. **d**, Precision primer extension analysis of the same 23S rRNA samples in the presence of dATP, dCTP, dTTP and ddGTP. The extent of Cfr-mediated methylation of the 23S rRNA (~70%) is calculated as the ratio of the intensity of the U2504-specific band to the sum of the intensities of the U2504- and C2501-specific bands and the readthrough bands (marked with an asterisk) after background subtraction. Experiments were repeated three times independently with similar results. SAM, S-adenosyl-L-methionine.

(NPET)[7–9]. The A2503 residue is also *C*-methylated at position 2 by the housekeeping rRNA-methylase RlmN (Fig. 1a), an enzyme widely distributed among bacteria[10]. RlmN and Cfr are homologs, sharing 34% sequence identity (*E. coli* RlmN versus *Staphylococcus aureus* Cfr), and both employ *S*-adenosyl methionine as methyl donor[11,12]. RlmN-mediated C2-methylation of A2503 is constitutively present in 23S rRNA and contributes to translational fidelity[13–15], whereas Cfr-mediated C8-methylation of the same nucleotide leads to multi-drug resistance[7,16].

The plasmid-borne *cfr* gene was first discovered in 2000 in the bacterial species *Mammaliicoccus sciuri* (previously *Staphylococcus sciuri*)[17] and was later found on plasmids in isolates from other sources[18]. In 2007, the first case of *cfr* occurrence in humans was identified in a clinical strain of methicillin-resistant *S. aureus* (MRSA, strain CM05), where the *cfr* gene was located on the chromosome[19]. Today, the *cfr* gene, with only minor sequence variations, has been found worldwide in pathogenic Gram-positive and Gram-negative bacteria isolated from humans and animals[4,5,20].

Based on a recent structure of the drug-free Cfr-modified 50S ribosomal subunit from *E. coli*[21], the observed effect of A2503-C8-methylation on the binding of some PTC-targeting antibiotics can be explained with a 'direct steric clash' model. Alignments of this Cfr-modified ribosome with those of various ribosome-bound PTC inhibitors show that the newly introduced C8-methyl group in A2503 sterically overlaps with the binding sites of many classes of PTC-acting drugs. Therefore, it has been proposed that the Cfr-dependent A2503-C8-methylation is likely to interfere physically with antibiotic binding[21].

However, we hypothesized that for some classes of antibiotics, the mechanism of Cfr-mediated resistance could also involve allosteric structural rearrangement(s) in the PTC that further reduces the antibiotic's binding affinity when aminoacyl- and/or peptidyl-tRNA ligands are present on the ribosome. The rationale for this hypothesis stems from the observation that key functional nucleotides around the PTC (A2062, U2506, U2585, A2602) change their positions upon binding of the tRNA substrates[22,23]. Importantly, one of these nucleotides (A2062) rotates relative to its position in a vacant ribosome in the presence of formyl-methionyl- or peptidyl-tRNA in the P site and forms a symmetric *trans* A–A Hoogsteen base pair with the residue A2503 (refs. 24–26). Thus, it is conceivable that Cfr-mediated C8-methylation of A2503 could allosterically affect the positions of other 23S rRNA nucleotides (such as A2062) in the presence of tRNAs, resulting in their

conformations being incompatible with a drug binding to its functional site in the PTC. Although an attractive hypothesis, such Cfr-dependent structural rearrangements have not been evaluated to date.

To understand the structural basis of Cfr-mediated resistance, we first identified conditions for expressing a functionally active Cfr methylase in the thermophilic bacterium *Thermus thermophilus* and solved the high-resolution X-ray crystal structure of the Cfr-modified 70S ribosome with nonhydrolyzable aa-tRNAs in both the A and P sites of the PTC. Using our recently developed approach for the semisynthesis of nonhydrolyzable peptidyl-tRNAs, we also solved the crystal structure of the Cfr-modified 70S ribosome with a peptidyl-tRNA in the P site. The structures reported herein reveal an unexpected Cfr-induced displacement of nucleotide A2062, which is likely to contribute to the mechanism of Cfr-based resistance resulting in the inability of PTC inhibitors to bind to the ribosome. Lastly, we determined the structure of the Cfr-modified 70S ribosome in complex with two antibiotics, iboxamycin (IBX) and tylosin (TYL), that exhibit activity against Cfr-expressing bacteria and uncovered the structural bases behind their abilities to engage the Cfr-modified ribosome. Notably, we observe a displacement of the Cfr-methylated A2503 nucleotide by ~1–1.5 Å upon binding of IBX, which could not have been predicted on the basis of existing antibiotic–ribosome co-crystal structures. Moreover, we have also found that, unlike IBX, TYL strongly engages 23S rRNA at a site distal from the site of Cfr-modification, allowing it to avoid a steric clash with the C8-methylated nucleotide A2503 by reorienting its mycarose sugar. Together, these examples illustrate two distinct mechanisms which allow antibiotics to maintain binding with Cfr-modified ribosomes and thus exhibit in vitro activity against some Cfr-expressing bacteria.

Results

Engineering of Cfr-expressing *T. thermophilus* strain

Cfr enzymes are expressed in a broad spectrum of pathogenic bacterial clinical isolates as well as in nonpathogenic bacteria, where they provide strong resistance to numerous PTC inhibitors[7,8,18–20]. As nucleotide A2503 of the 23S rRNA is inaccessible to enzymes in the mature 50S subunit, RlmN and Cfr methylases must operate during the ribosome assembly process[11]. Therefore, to isolate predominantly Cfr-modified ribosomes for crystallographic study, we first constructed a bacterial strain expressing a catalytically active Cfr methylase.

Based on our past work in obtaining Erm-modified 70S ribosomes (containing N6-dimethyl-adenine at position 2058 of the 23S rRNA) and solving its high-resolution structure[24], we have chosen the same Gram-negative thermophilic bacterium *T. thermophilus* (*Tth*) as our experimental model. Because expression of a functionally active Cfr enzyme from the mesophilic bacterium *S. aureus* in the thermophilic bacterium *Tth* is unlikely to be successful, we selected five *cfr*-like genes from genomes of bacteria adapted for growth at elevated temperatures and used the *cfr* gene from *S. aureus* as a control (Supplementary Figs. 1 and 2 and Supplementary Table 1). The desired *cfr*-like genes were commercially synthesized, cloned into the previously assembled pBGAA1-BthERM vector (Fig. 1b, top) to replace the *erm* gene[24] (Fig. 1b, bottom) and expressed in *Tth* HB27 cells.

Cfr expression in the resulting strains was first assessed by a microbiological approach that exploits the sensitivity of wild-type (WT) *Tth* cells to several well-characterized PTC-targeting drugs, such as chloramphenicol (CHL), lincomycin (LNC) and clindamycin (CLI). Antibiotic susceptibility testing of the plasmid-transformed *Tth* cells showed that the expression of a *cfr*-like gene from *Planifilum fimeticola* (referred to hereafter as PfiCFR) or *Planifilum fulgidum* (PfuCFR) resulted in a substantial increase of minimal inhibitory concentrations (MICs) for CHL, LNC and CLI by 32-, 1,024- and 4,096-fold, respectively (Supplementary Table 2, red), when compared with control cells carrying an empty vector (Supplementary Table 2, blue). In contrast, the MICs for the NPET-targeting macrolide erythromycin remained unchanged (Supplementary Table 2, green), representing a resistance phenotype consistent with *cfr* expression.

To further verify that the observed drug resistance arose from the specific methylase activity of PfuCFR, we used a primer extension assay to assess A2503 modifications biochemically. This method is based on the arrest of reverse transcriptase progression on the rRNA template due to its inability to incorporate a complementary nucleotide into the synthesized complementary DNA at the position complementary to or preceding the methylated adenine. Since nucleotide A2503 in the WT 70S ribosome is already methylated at position C2 by the housekeeping rRNA-methylase RlmN, we expected the cDNA arrest product to be observed even in the case of 23S rRNA isolated from WT *Tth* cells. Therefore, we used 23S rRNA isolated from a *Tth* HB27 *rlmN*$^-$ strain lacking A2503-C2-methylation as a reference and negative control. By optimizing the concentrations of nucleotides and reverse transcriptase enzymes, as well as reaction time, we developed primer extension reaction conditions that allowed us to differentiate between unmodified (*rlmN*$^-$), C2-monomethylated (WT) and C2,C8-dimethylated (*cfr*$^+$) adenine nucleotides at position 2503 of the 23S rRNA (Fig. 1c,d, lanes 2, 3 and 4, respectively). As expected, the strongest reverse transcription arrest was observed for the 23S rRNA isolated from the *cfr*-positive *Tth* cells (Fig. 1c, lane 4), confirming that PfuCFR modifies the desired A2503 residue in the 23S rRNA. Next, to quantitatively assess the extent of C8-methylation of A2503, we performed precision primer extension analysis of the same 23S rRNA samples in the presence of dATP, dCTP, dTTP and ddGTP. While the dideoxynucleotide ddGTP causes reverse transcription to stop at position C2501 on all templates, the Cfr-catalyzed C8-methylation of m^{2}A2503 causes arrest of cDNA synthesis at the preceding position U2504 of the 23S rRNA (Fig. 1d), likely due to the inability of reverse transcriptase to accommodate modified adenine nucleotides in its active site. Thus, the ratio of intensities of U2504-specific bands to the sum of U2504- and C2501-specific bands provides the extent of Cfr-methylation. By optimizing the growth conditions of the PfuCFR-expressing *Tth* strain, we achieved levels of A2503-C8-methylation as high as 70% (Fig. 1d, lane 4). Altogether, our microbiological and biochemical data show that the Cfr homologs from *P. fimeticola* and *P. fulgidum* possess the desired activities and can be expressed in *Tth* HB27 cells to modify the m^{2}A2503 residue in the bacterial 23S rRNA.

Structure of the 70S ribosome containing m^{2}m^{8}A2503

We purified 70S ribosomes from the *Tth* HB27 strain expressing PfuCFR-methylase for structural analysis. To assess if the presence of aa-tRNA substrates affects the position of C8-methylated nucleotide A2503, we used these Cfr-modified *Tth* 70S ribosomes to assemble a complex with Phe-tRNA^{Phe} and fMet-tRNA$_i^{Met}$ in the A and P sites, respectively. The complex was crystallized using previously published conditions[23–27], and its structure was determined at 2.55-Å resolution (Supplementary Table 3). At this resolution, nucleotide methylations can be directly visualized in the unbiased difference electron density maps (Fig. 2a, green mesh), allowing for accurate modeling of the C2,C8-dimethylated nucleotide A2503 (m^{2}m^{8}A2503) of the 23S rRNA in the structure (Fig. 2a,b). Additionally, by using nonhydrolyzable, amide-linked aa- and peptidyl-tRNAs in our ribosome complexes (Methods), we were able to capture the PTC in its pre-transpeptidation state.

We aligned our structure of the 70S ribosome containing Cfr-methylated m^{2}m^{8}A2503 with a structure of the 70S ribosome containing WT m^{2}A2503 (Extended Data Fig. 1a,b)[24] to search for any Cfr-induced structural rearrangements around the PTC that could result in multidrug resistance. Consistent with the recent structure of a Cfr-modified *E. coli* 70S ribosome by the Fujimori group (Extended Data Fig. 1e,f)[21,28], our structure reveals that C8-methylation does not affect the overall position of nucleotide A2503 in the Cfr-modified ribosome (Extended Data Fig. 1a,b). Moreover, the alignment revealed no major changes in either the positions of the A- and P-site tRNA

https://doi.org/10.1038/s41589-023-01525-w

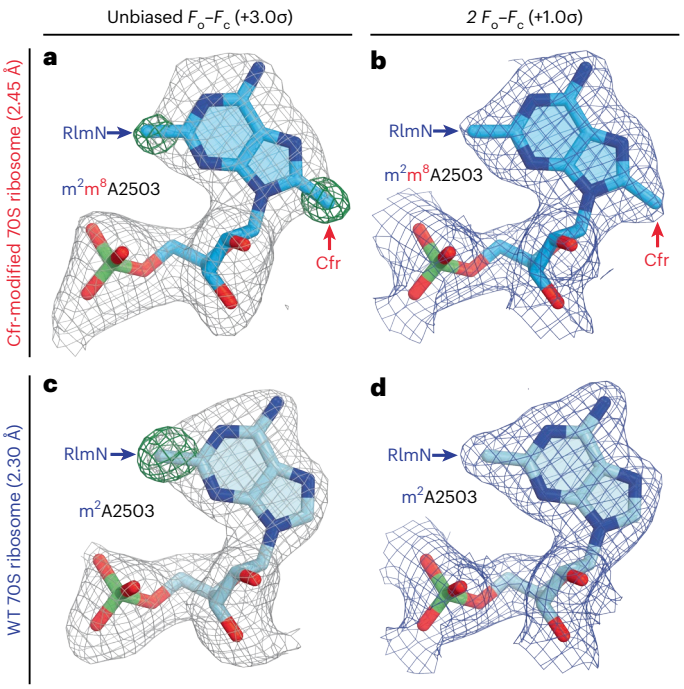

Fig. 2 | Electron density maps of C2,C8-dimethylated (top) and C2-methylated (bottom) A2503 residue of the 23S rRNA in *T. thermophilus* 70S ribosome. **a**–**d**, Unbiased F_o–F_c (**a**,**c**) (gray and green mesh) and 2F_o–F_c (**b**,**d**) (blue mesh) electron difference Fourier maps of nucleotide A2503 in the *T. thermophilus* 70S ribosome contoured at 3.0σ and 1.0σ, respectively. Gray mesh shows the F_o–F_c map after refinement with the entire modified nucleotide omitted. Green mesh, reflecting the presence of methyl groups, shows the F_o–F_c electron density map after refinement with the nucleotide A2503 built as a regular unmethylated adenine. The refined models of Cfr-modified C2,C8-dimethylated (**a**,**b**) or WT RlmN-modified C2-methylated (**c**,**d**) A2503 nucleotide are displayed in the corresponding electron density maps. The structure and the electron density maps of the WT ribosome complex (**c**,**d**) are from PDB entry 6XHW (ref. 24). Carbon atoms are colored blue for the Cfr-modified A2503 and light blue for the C8-unmethylated A2503; nitrogens are dark blue, oxygens are red and phosphorus atoms are green.

substrates (Extended Data Fig. 1b) or most of the key functional nucleotides of the 23S rRNA around the PTC (Extended Data Fig. 1a). However, we observed an unanticipated conformational change of nucleotide A2062. In all previous WT ribosome structures containing aminoacylated Phe-tRNA^{Phe} and fMet-tRNA$_i^{Met}$ in the A and P sites, respectively, nucleotide A2062 is always observed in its rotated conformation (Extended Data Figs. 2a and 3a) and forms direct van der Waals interactions with the formyl-methionyl moiety of the P-site tRNA[24]. In our structure, however, the electron density corresponding to A2062 was relatively weak (Extended Data Fig. 3b), indicating low conformational stability, and the modeled A2062 lacked the characteristic rotation and Hoogsteen base-pairing with nucleotide m^{2}m^{8}A2503 (Extended Data Fig. 1a).

Cfr-mediated methylation of m^{2}A2503 prevents A2062 rotation

In our recently published structures of WT *Tth* ribosomes featuring full-length peptidyl-tRNAs[25,26] or their short analogs[29] in the P site, nucleotide A2062 is always observed in its rotated conformation and forms an additional H-bond with the amide of the penultimate amino acid residue of the peptidyl-tRNA (Extended Data Fig. 4a,b). Therefore, we reasoned that if A2062 remained unrotated in the Cfr-methylated ribosome despite the potential for an additional stabilizing H-bond with the peptidyl-tRNA, then this structural evidence would strongly support our hypothesis that Cfr-mediated methylation precludes the Hoogsteen base-pairing of A2062 with m^{2}m^{8}A2503. To unambiguously determine the conformation of A2062 in the Cfr-modified ribosome and further investigate A2062's inability to form a Hoogsteen base pair with m^{2}m^{8}A2503, we solved the structure of a Cfr-methylated 70S ribosome with peptidyl-tRNA in place of fMet-aminoacyl-tRNA$_i^{Met}$ in the P site.

Using our recently developed chemoenzymatic approach based on native chemical ligation[26], we prepared a nonhydrolyzable peptidyl-tRNA carrying a formyl-Met-Thr-His-Ser-Met-Arg-Cys (fMTHSMRC) heptapeptide moiety. In the previously reported structure of the same peptidyl-tRNA in complex with WT 70S ribosome[26], the rotated conformation of nucleotide A2062 was stabilized not only by direct H-bonding with the fMTHSMRC-peptide moiety (Extended Data Fig. 4a,b) but also by π–π stacking with the imidazole side chain of the His3 residue (Extended Data Fig. 4b). Using this peptidyl-tRNA as the P-site substrate, we assembled a complex of Cfr-modified *Tth* 70S ribosome containing Phe-tRNA^{Phe} in the A-site and solved its structure at 2.45-Å resolution (Fig. 3a–d and Supplementary Table 3). Similar to the structure with P-site fMet-tRNA$_i^{Met}$, we observed no major changes in the positions of 23S rRNA nucleotides (Extended Data Fig. 1c) or the A- or P-site tRNA bodies (Extended Data Fig. 1d). However, unlike the structure with P-site fMet-tRNA$_i^{Met}$, the electron density for the A2062 nucleotide became well-defined in the structure with P-site peptidyl-tRNA (Fig. 3c,d and Extended Data Fig. 3c), allowing us to determine its position and orientation unequivocally. Remarkably, despite the potential for stabilizing interactions with the peptidyl-tRNA, nucleotide A2062 remained in its unrotated conformation (Fig. 3d–f and Extended Data Fig. 1c), suggesting that Cfr-mediated methylation of m^{2}A2503 renders it unable to form a symmetrical Hoogsteen base pair with A2062. This observation is further supported by analysis of recently published cryo-electron microscopy structures of WT (Extended Data Fig. 5a) and Cfr-modified *E. coli* 70S ribosomes (Extended Data Fig. 5b)[28], where A2062 is also observed without rotation and base-pairing with m^{2}m^{8}A2503. Besides A2062, no other structural rearrangements of 23S rRNA nucleotides are visible in the PTC (Extended Data Fig. 1c).

Mechanisms of Cfr-mediated resistance to PTC-acting drugs

Cfr-class methylases have been generally accepted to confer resistance to PTC-targeting ribosomal antibiotics by introducing a methyl group to the C8-atom of the nucleotide m^{2}A2503, a modification that protrudes into the common binding pocket occupied by these antibiotic classes. Superpositions of the Cfr-modified *Tth* ribosome structure with those of the WT ribosome bound by various PTC-targeting drugs reveal overlaps between the C8-methyl group of m^{2}m^{8}A2503 and the drug molecules (Fig. 4 and Extended Data Fig. 8), supporting the prevailing 'direct steric clash' model. However, this analysis shows a relatively small extent of steric overlap (0.4–0.5 Å) between the C8-methyl group of m^{2}m^{8}A2503 and several PTC-binding drugs, such as CHL (Fig. 4a, 0.4 Å), linezolid (Fig. 4b, 0.5 Å) and hygromycin A (Fig. 4c, 0.5 Å). In published structures of ribosome-bound phenicols[25,29–32], oxazolidinones[28] and hygromycin A[9], we consistently observed the Hoogsteen base-pairing of nucleotide A2062 with m^{2}A2503, which enables a direct H-bond between the N6-atom of A2062 and the bound antibiotic. We thus hypothesized that the inability of A2062 to rotate in the Cfr-modified ribosome could prevent additional binding interactions between the antibiotic and 23S rRNA, thereby contributing to drug resistance for these antibiotic classes via an allosteric mechanism.

To test this hypothesis, we determined MICs of different PTC-targeting antibiotics against a panel of antibiotic-hypersensitive *E. coli* SQ171 Δ*tolC* strains[33] that lack all the chromosomal *rrn* operons and instead carry a plasmid-encoded WT or A2062G/U/C-mutant versions of the 23S rRNA gene (Supplementary Table 4). In the A2062G

https://doi.org/10.1038/s41589-023-01525-w

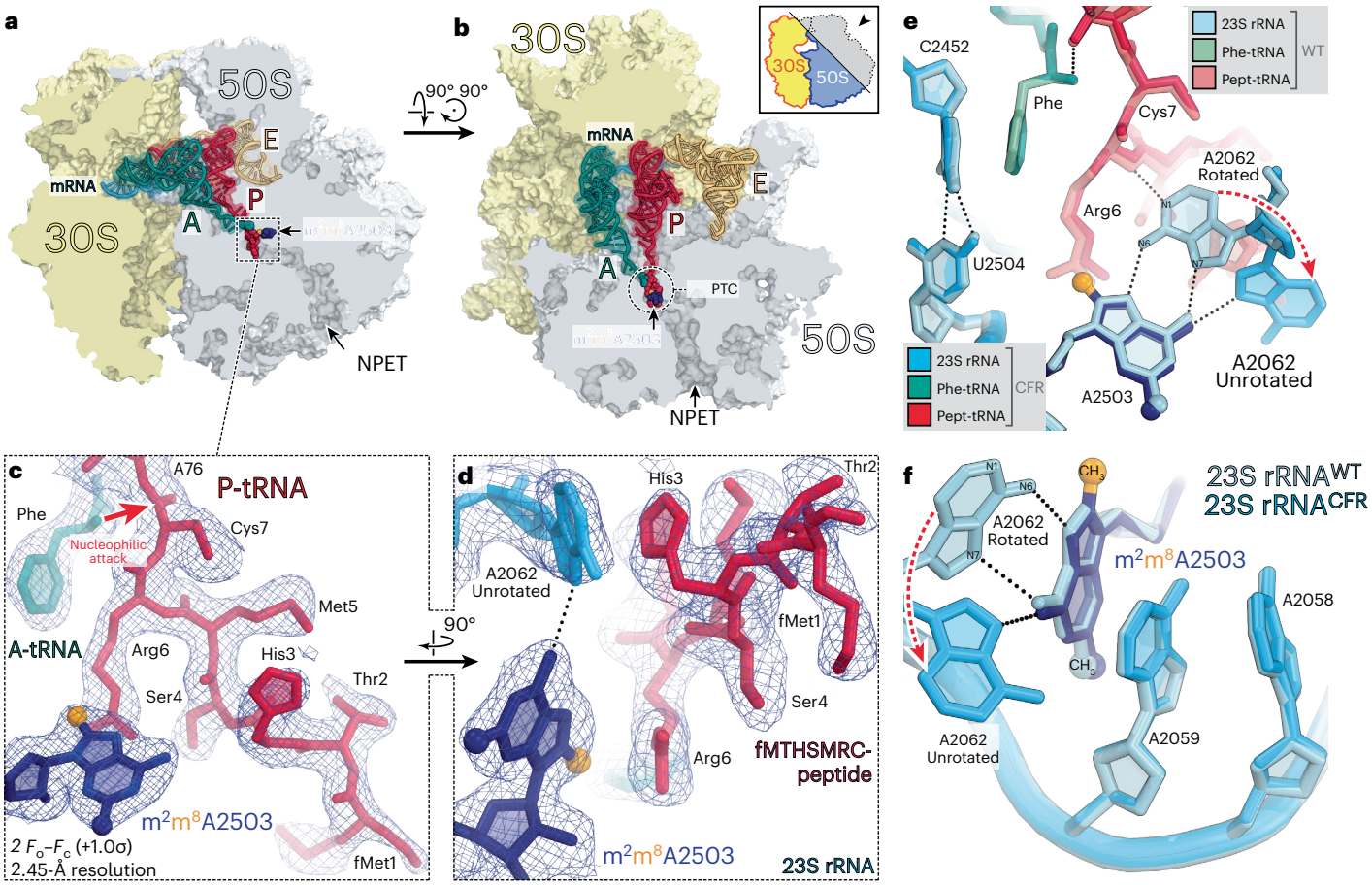

Fig. 3 | Structure of the Cfr-modified 70S ribosome. a,**b**, Location of the Cfr-modified nucleotide A2503 (navy blue) carrying the C8-methyl group (orange) in the PTC of the *Tth* 70S ribosome relative to tRNAs viewed from two different angles as cross-cut sections through the NPET. The 30S subunit, 50S subunit and mRNA are colored light yellow, light blue and blue, respectively, while the A-, P- and E-site tRNAs are colored teal, crimson and light orange, respectively. **c**,**d**, Close-up views of the $2F_o–F_c$ electron density map (blue mesh) of m^2m^8A2503 nucleotide and ribosome-bound A-site Phe-tRNA^{Phe} (teal) and P-site fMTHSMRC-peptidyl-tRNA$_i^{Met}$ (crimson). **e**,**f**, Superpositioning of the previously reported structure of WT 70S ribosome containing A-site Phe-tRNA^{Phe} and P-site fMTHSMRC-peptidyl tRNA$_i^{Met}$ (PDB entry 8CVL (ref. 26)) with the structure of the same complexes containing Cfr-methylated nucleotide m^2m^8A2503 in the 23S rRNA. Nucleotides of the Cfr-modified and unmodified ribosomes are shown in blue and light blue, respectively. All structures were aligned based on domain V of the 23S rRNA. *E. coli* nucleotide numbering is used throughout. H-bonds are shown with dotted lines. Pept-tRNA, peptidyl-tRNA.

mutant strain, the guanosine at position 2062 would no longer be able to rotate and form a Hoogsteen base pair with m^2A2503 but would still be able to maintain the H-bonding interaction between its N7 and the exocyclic N–H of m^2A2503 in its unrotated conformation (Extended Data Fig. 2b). We believe that this mutation would prevent nucleotide rotation at position 2062 without methylation at C8 of m^2A2503, allowing us to assess the relative contribution from the proposed allosteric component of Cfr-mediated resistance. When CHL, florfenicol, linezolid and hygromycin A were assessed against this A2062G mutant strain, a 2- to 16-fold MIC increase was recorded compared with WT (Supplementary Table 4). In contrast, the activities for CLI and IBX were unaffected or even potentiated by the A2062G mutation, though a fourfold increase in MIC was observed for LNC (Supplementary Table 4). When the same antibiotic panel was assessed against *cfr*-expressing *T. thermophilus* or *S. aureus* cells, a 16- to 32-fold increase in MICs was observed for CHL, florfenicol, linezolid and hygromycin A compared with the parent strains (Supplementary Table 5). In contrast, the activity of all lincosamide derivatives (LNC, CLI, IBX) decreased substantially (≥64 to 4,096-fold) upon expression of *cfr* (Supplementary Table 5). These data suggest that, for at least phenicol and oxazolidinone antibiotics, a substantial portion of Cfr-mediated resistance may be driven by the inability of A2062 to rotate and form additional stabilizing interactions with the bound antibiotic.

In contrast to the A2062G mutation, the substitutions of nucleotide A2062 with pyrimidines (U or C), which are unable to interact with m^2A2503 similarly to A2062, results in strong resistance to most A-site targeting antibiotics (such as CHL, linezolid, hygromycin A, LNC or CLI), suggesting the importance of this nucleotide for drug engagement with the ribosome (Supplementary Table 4). However, lacking the corresponding structures of the A2062-mutant ribosomes, we cannot exclude the possibility of other changes occurring in the PTC as a direct consequence of these mutations. Notably, the 16MMs, spiramycin and josamycin, were also affected by all three A2062G/U/C mutations (Supplementary Table 4). However, this decrease in potency is likely due to the loss of a covalent linkage to A2062, which is generally required for their activity[34]. Altogether, our structural analysis and microbiological data suggest that the mechanism of Cfr-mediated resistance to certain PTC-targeting antibiotics appears to be two-component: (1) direct steric hindrance with the drug molecules and (2) allosteric rearrangement of the drug binding pocket.

How antibiotics engage the Cfr-modified ribosome

Although the C8-methylation of A2503 leads to high levels of resistance against a range of PTC-targeting antibiotics, including lincosamides, some continue to exhibit activity against *cfr*-positive pathogens. The recently disclosed oxepanoprolinamide antibiotic IBX engages

https://doi.org/10.1038/s41589-023-01525-w

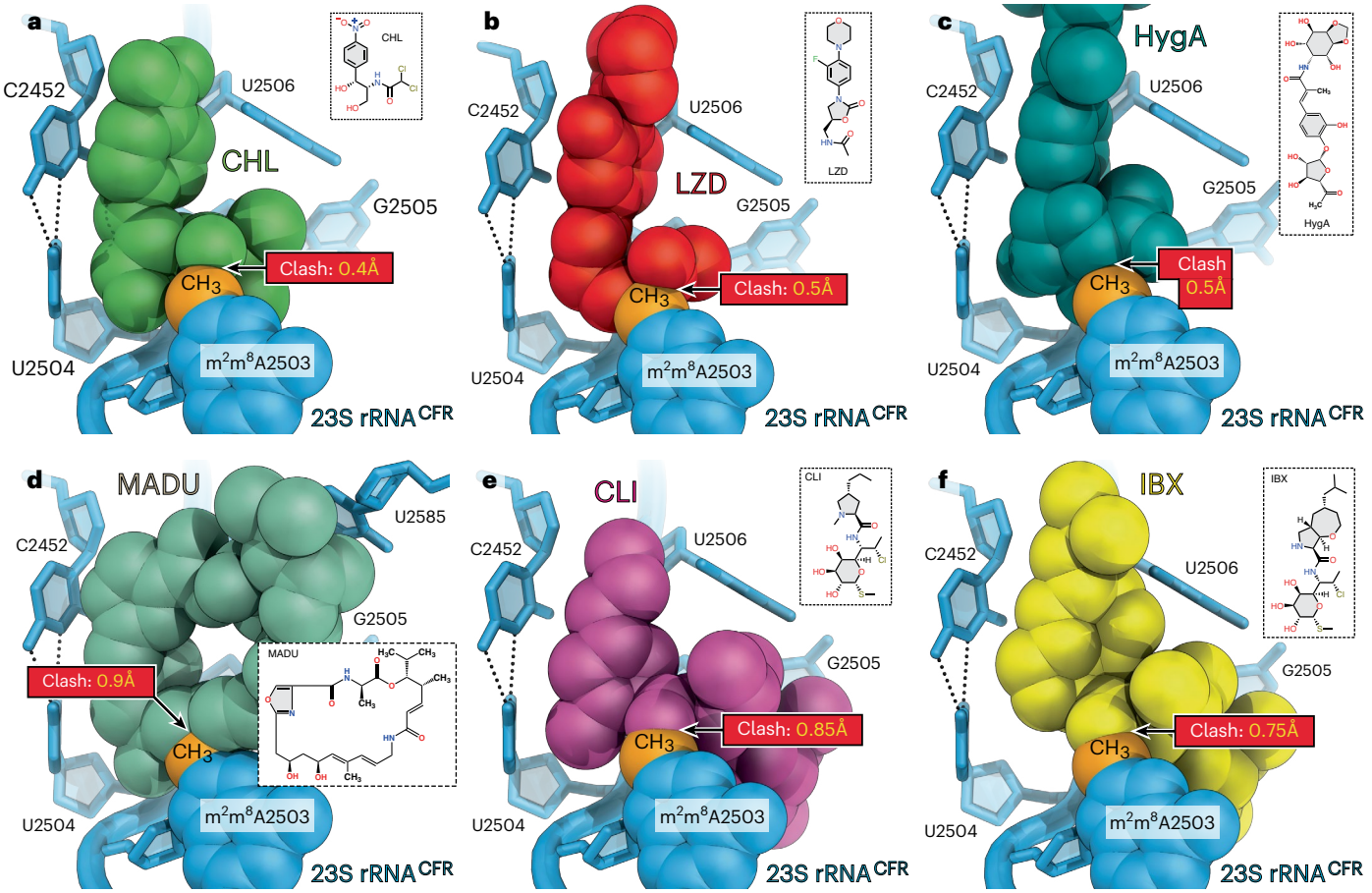

Fig. 4 | Structural basis for Cfr-mediated resistance to PTC-acting antibiotics. **a**–**f**, Superpositions of the structure of Cfr-modified *T. thermophilus* 70S ribosome containing m^2m^8A2503 nucleotide (blue with the C8-methyl group in orange) in the 23S rRNA with the structures of WT ribosome-bound antibiotics targeting the PTC: CHL (**a**, green, PDB entry 7RQE (ref. 29)), linezolid (**b**, LZD, red, PDB entry 7S1G (ref. 28)), hygromycin A (**c**, HygA, teal, PDB entry 5DOY (ref. 9)), madumycin (**d**, MADU, light teal, PDB entry 5VP2 (ref. 43)), CLI (**e**, magenta, PDB entry 4V7V (ref. 44)) and IBX (**f**, yellow, PDB entry 7RQ8 (ref. 36)). The degrees of steric overlaps between the C8-methyl group of the m^2m^8A2503 nucleotide and each of the PTC-acting drugs are shown in yellow. These numbers reflect the distance in Å that the drug and the m^2m^8A2503 residue need to move away from each other to avoid steric clash. Note that the C8-methyl group of m^2m^8A2503 can physically interfere with the binding of chemically unrelated antibiotic classes.

the bacterial ribosome with strong affinity[35] and exhibits a broad spectrum of activity in high-priority Gram-positive pathogens[36]. Importantly, IBX maintains demonstrable activity against Gram-positive strains harboring Erm-, ABCF- (ATP-binding cassette type F proteins) or Cfr-resistance determinants[36], although less so against the synergetic protection via 23S modification by Erm/Cfr and direct protection by ABCFs[37,38].

Upon superposition of the Cfr-modified ribosome with ribosome-bound IBX or CLI, the amide moiety of each antibiotic is expected to exhibit a similar steric clash with the C8-methyl group of m^2m^8A2503 (Fig. 4e,f). However, in vitro susceptibility testing against *cfr*-expressing strains shows that IBX is substantially less affected by the expression of *cfr* (32–64× MIC increase, Supplementary Table 5) than canonical lincosamides such as LNC (512–1,024× MIC increase, Supplementary Table 5) or CLI (4,096× MIC increase, Supplementary Table 5)[36]. Simple structural comparison between the antibiotics cannot readily rationalize this increased activity, as the amide moiety remains unchanged between IBX and CLI (Fig. 4e,f). Therefore, a deeper understanding of how IBX maintains interactions with the A2503-C8-methylated ribosome is critical for informing the development of antibiotics with enhanced activity against *cfr*-positive pathogens.

To uncover the structural basis for IBX's activity in *cfr*-expressing pathogens, we determined its structure in complex with the Cfr-modified ribosome at 2.55-Å resolution (Fig. 5a,b, Extended Data Fig. 6 and Supplementary Table 3). Similar to CLI, a network of H-bonds anchors the aminooctose moiety of IBX to nucleotides A2058, A2059 and A2503 in the NPET (Fig. 5c). However, unlike traditional lincosamides, the bicyclic framework of IBX projects an isobutyl moiety from C7′, conferring additional engagement of the PTC by extending deep into the A-site cleft[36]. This hydrophobic cleft, formed by the 23S rRNA residues A2451 and C2452, normally accommodates side chains of incoming amino acids and plays a key role in positioning the aminoacylated 3′-end of A-site tRNA within the PTC during transpeptidation[23,26]. Remarkably, the observed electron density map reveals that the binding site of IBX in the Cfr-methylated ribosome is nearly identical to that in the WT ribosome (Fig. 5c,d), whereas m^2m^8A2503 undergoes a movement of ~1–1.5 Å relative to its canonical position to accommodate the antibiotic (Fig. 5d). This displacement of m^2m^8A2503, which also disrupts one H-bond typically formed between 2′-OH of A2503 and the aminooctose group of lincosamides (Fig. 5d and Extended Data Fig. 7), is not a trivial concession to make since it is clearly sufficient to disrupt CLI binding. However, the extended hydrophobic interaction between IBX and the A-site cleft compensates for this clash with the m^2m^8A2503 nucleobase, providing sufficient affinity to engage Cfr-modified ribosomes, albeit with higher MIC values in vitro (Supplementary Table 5).

Expression of *cfr* also confers resistance to some 16MMs, which bind in the canonical macrolide binding pocket located in the NPET[34].

https://doi.org/10.1038/s41589-023-01525-w

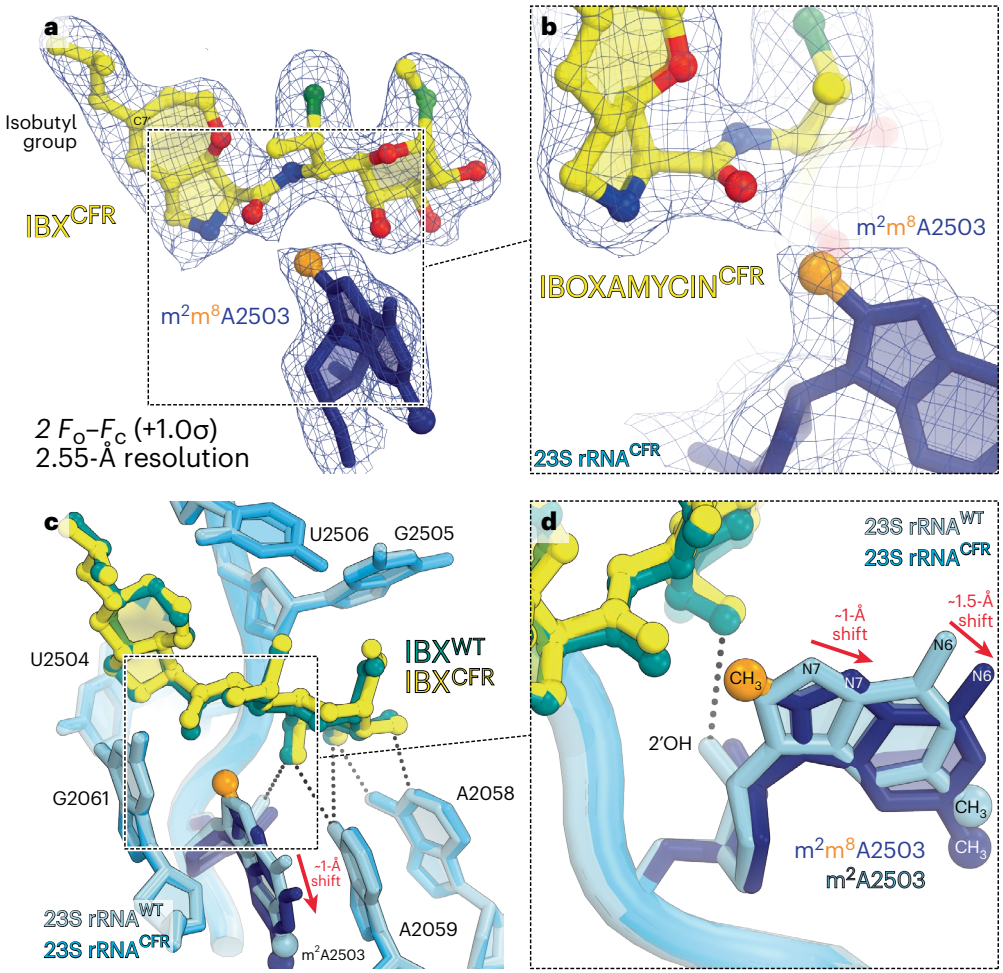

Fig. 5 | Structure of IBX bound to the Cfr-methylated 70S ribosome. **a**,**b**, Electron density map (blue mesh) contoured at 1.0σ of IBX (yellow) in complex with the Cfr-modified *T. thermophilus* 70S ribosome containing m^2m^8A2503 nucleotide in the 23S rRNA (navy blue). The C8-methyl group of m^2m^8A2503 is highlighted in orange. **c**,**d**, Superposition of IBX (teal) in complex with the WT 70S ribosome containing a C8-unmodified residue m^2A2503 (light blue) and the structure of IBX (yellow) in complex with the Cfr-modified 70S ribosome containing an m^2m^8A2503 residue (navy blue). Hydrogen bonds are depicted with dotted lines. The structure of IBX in complex with the WT 70S ribosome (colored in teal in **c** and **d**) is from PDB entry 7RQ8 (ref. 36). Note that while the positions of IBX are almost identical in the two structures, the m^2m^8A2503 residue in the IBX-bound Cfr-modified structure is shifted by ~1–1.5 Å relative to the canonical position of the m^2A2503 residue of the WT ribosome with IBX bound (red arrows).

Unlike conventional 14-membered macrolides (such as erythromycin), these compounds extend further into the PTC with disaccharide projections (such as in TYL), with some reaching the A-site cleft through additional substitutions on the disaccharide (such as in josamycin)[34]. Cfr resistance can be attributed to these disaccharides, as alignments of our structure of the Cfr-modified 70S ribosome with the previous structures of 16MMs in complex with the *Haloarcula marismortui* 50S subunit[34] reveal a steric clash between the terminal mycarose moiety of 16MMs and the C8-methyl group of m^2m^8A2503 (Extended Data Fig. 8). Although Cfr confers strong (up to 64-fold) resistance to 16MMs such as spiramycin and josamycin (Supplementary Table 5 and ref. 8), it causes a ≤2-fold increase in MIC for TYL (Supplementary Table 5 and refs. 7,8), suggesting that TYL retains affinity for the Cfr-modified ribosome despite possessing the mycaminose-mycarose disaccharide conserved among these 16MMs. To experimentally elucidate TYL's mechanism for overcoming the modeled steric clash, we determined the structure of TYL in complex with Cfr-modified ribosomes, with Phe-tRNA^{Phe} and fMet-tRNA$_i^{Met}$ in the A and P sites, respectively. The 2.65-Å electron density map revealed TYL bound in the canonical macrolide NPET binding pocket with the Cfr-modified m^2m^8A2503 nucleotide (Fig. 6a, Extended Data Fig. 9a–c and Supplementary Table 3). Consistent with the previous 3-Å structure of TYL in complex with an A2503-unmodified, ligand-free 50S subunit from the archaeon *H. marismortui*[34], the acetaldehyde moiety at C6 of TYL forms a covalent bond with the exocyclic N6-amino group of A2062 in the *Tth* ribosome, as manifested by the continuous electron density connecting the drug to the nucleobase (Extended Data Fig. 9b). To accurately evaluate the effect of Cfr-mediated methylation on the position of TYL in the Cfr-modified ribosome, we also determined its structure in complex with the unmodified WT *Tth* 70S ribosome (Fig. 6a, Extended Data Fig. 9d–f and Supplementary Table 3). Alignment of our structures of Cfr-modified ribosomes, with and without TYL bound, reveals neither displacement of nucleotide m^2m^8A2503 nor any structural rearrangements elsewhere in the 23S rRNA (Extended Data Fig. 10c,d). However, a comparison between structures of TYL bound to WT and Cfr-modified *Tth* ribosomes shows that, although TYL occupies the same overall binding site, the terminal mycarose moiety of TYL in the Cfr-modified ribosome is deflected away from the C8-methyl of m^2m^8A2503 to avoid a steric clash (Fig. 6b,c). This deflection is likely made possible by a key structural feature that distinguishes TYL from other 16MMs, namely, its mycinose sugar at position C14 of the macrolactone core (Extended Data Figs. 8a and 9d). In both the WT and Cfr-modified structures, this mycinose is observed in an identical position, engaging in

https://doi.org/10.1038/s41589-023-01525-w

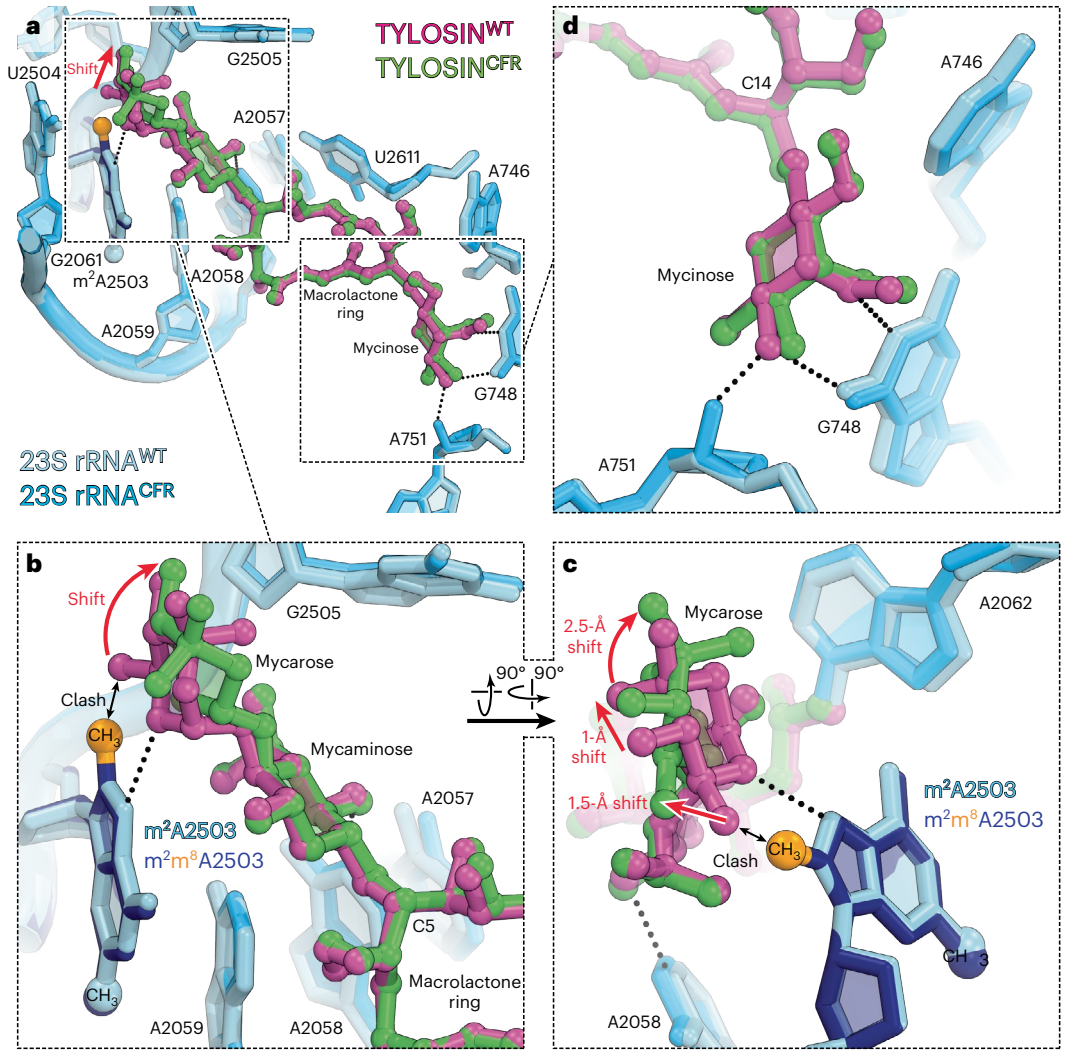

Fig. 6 | Comparison of the structures of TYL bound to the Cfr-modified and WT 70S ribosomes. a, Superposition of TYL (magenta) in complex with the WT 70S ribosome containing m^2A2503 residue (light blue) and the structure of TYL (green) in complex with the Cfr-modified 70S ribosome containing m^2m^8A2503 residue (navy blue). Hydrogen bonds are depicted with dotted lines. Note that the position of m^2m^8A2503 residue is almost identical in the two structures, whereas TYL binding to the Cfr-modified ribosome causes an ~1.5–2.5-Å shift of its mycarose moiety to a new position (red arrows). **b**, Close-up view of the C5-mycaminose-mycarose disaccharide moiety of TYL, which is shared by most 16MMs and is a key part of the general pharmacophore for macrolide binding. **c**, Rearrangement of the TYL's mycarose moiety upon binding to the Cfr-modified ribosome. **d**, Interactions of the TYL's unique C14-mycinose moiety with the nucleotides of the 23S rRNA.

additional van der Waals and H-bond interactions with the 23S rRNA (Fig. 6d)[34]. These compensatory interactions likely provide sufficient target affinity for TYL to engage the Cfr-modified ribosome despite the apparent thermodynamic penalty for reorienting its mycaminose-mycarose moiety. The additional contacts of TYL with the ribosome provided by the C14-mycinose moiety may also explain TYL's reduced susceptibility to A2058 and A2059 mutations[39]. Moreover, it has been shown that disruption of the C14-mycinose interactions due to methylation of G748 by TlrB confers resistance to TYL when A2058 is also N6-monomethylated[40]. However, monomethylation at either position (G748 or A2058) is insufficient to afford protection[40], highlighting the importance of the mycinose fragment for the engagement of bacterial ribosomes by TYL. Furthermore, cross-resistance to TYL is conferred by Erm methyltransferases[8], ruling out a secondary mechanism of action for its antibacterial activity. Since spiramycin and josamycin lack this mycinose anchor, we speculate that these molecules cannot leverage the same reorientation as TYL to maintain target engagement with Cfr-modified ribosomes.

Discussion

Altogether, our structural study of Cfr-mediated resistance to PTC-targeting ribosomal antibiotics suggests that the underlying mechanism of resistance at the molecular level appears to be two-component: (1) direct steric hindrance of the A2503-C8-methyl group with the ribosome-bound drugs; and (2) Cfr-methylation-induced rearrangement of the nucleotide A2062 to a conformation incompatible with drug binding. Although the relative contributions of these two mechanisms vary depending on the particular antibiotic, together they ensure that a single methyl group added to the A2503 residue in a 2.5-MDa ribosome renders many chemically unrelated classes of antibiotics unable to bind to such ribosomes. The structure of IBX in complex with the Cfr-modified ribosome reveals an unexpected finding: by establishing strong contacts with the 23S rRNA, IBX is able to displace m^2m^8A2503 from its canonical position, thereby engaging Cfr-modified ribosomes. The displacement of m^2m^8A2503 by IBX in Cfr-methylated ribosomes is conceptually reminiscent of the previously reported displacement of m_2^6A2058 by IBX in Erm-methylated ribosomes[36]. This unanticipated nucleotide mobility further underscores the ability of

a synthetic antibiotic to overcome methylase-mediated resistance by compensating with binding affinity from proximal interactions, going against conventional principles of small-molecule inhibitor design. Thus, forming new interactions with the ribosomal A site may prove a general strategy in the design of antibiotics with increased activity against both *cfr*- and *erm*-expressing pathogens.

In contrast to IBX, TYL engages the Cfr-modified ribosome by reorienting its terminal mycarose sugar to avoid steric clash with m^2m^8A2503. The apparent flexibility of the mycarose moiety is likely made possible by additional contacts afforded by TYL's mycinose sugar, which differentiates it from other 16MMs such as spiramycin and josamycin. The apparent flexibility of TYL when engaging the Cfr-modified ribosome is in striking contrast to IBX, which instead displaces m^2m^8A2503 from its canonical position in the PTC. Thus, IBX and TYL illustrate two distinct mechanisms that may allow antibiotics to maintain binding to Cfr-modified ribosomes: (1) strong target engagement resulting in displacement of the Cfr-methylated m^2m^8A2503 nucleotide, as in the case of IBX; or (2) strong target engagement in one part of the drug molecule allowing for distal positional readjustments to avoid clashes with the m^2m^8A2503 nucleotide, as in the case of TYL. In summary, strong binding interactions distal to the site of Cfr-mediated methylation can allow an antibiotic to take advantage of its inherent flexibility (or the ribosome's flexibility) to engage the Cfr-methylated ribosome efficiently.

We believe that the information provided by the structure of the Cfr-modified ribosome and its complexes with antibiotics is an essential starting point for the structure-based development of next-generation drugs active against the most challenging multidrug-resistant pathogens. This quest will likely be stimulated by the recently discovered combinatorial approaches for the synthesis of novel oxepanoprolinamides[36], streptogramins[41], pleuromutilins[42] and other antibiotics.

Online content

Any methods, additional references, Nature Portfolio reporting summaries, source data, extended data, supplementary information, acknowledgements, peer review information; details of author contributions and competing interests; and statements of data and code availability are available at https://doi.org/10.1038/s41589-023-01525-w.

References

1. Wilson, D. N. The A-Z of bacterial translation inhibitors. *Crit. Rev. Biochem. Mol. Biol.* **44**, 393–433 (2009).
2. Wilson, D. N. Ribosome-targeting antibiotics and mechanisms of bacterial resistance. *Nat. Rev. Microbiol.* **12**, 35–48 (2014).
3. Lin, J., Zhou, D., Steitz, T. A., Polikanov, Y. S. & Gagnon, M. G. Ribosome-targeting antibiotics: modes of action, mechanisms of resistance, and implications for drug design. *Annu. Rev. Biochem.* **87**, 451–478 (2018).
4. Shen, J., Wang, Y. & Schwarz, S. Presence and dissemination of the multiresistance gene cfr in Gram-positive and Gram-negative bacteria. *J. Antimicrob. Chemother.* **68**, 1697–1706 (2013).
5. Vester, B. The cfr and cfr-like multiple resistance genes. *Res. Microbiol.* **169**, 61–66 (2018).
6. Giessing, A. M. et al. Identification of 8-methyladenosine as the modification catalyzed by the radical SAM methyltransferase Cfr that confers antibiotic resistance in bacteria. *RNA* **15**, 327–336 (2009).
7. Long, K. S., Poehlsgaard, J., Kehrenberg, C., Schwarz, S. & Vester, B. The Cfr rRNA methyltransferase confers resistance to Phenicols, Lincosamides, Oxazolidinones, Pleuromutilins, and Streptogramin A antibiotics. *Antimicrob. Agents Chemother.* **50**, 2500–2505 (2006).
8. Smith, L. K. & Mankin, A. S. Transcriptional and translational control of the mlr operon, which confers resistance to seven classes of protein synthesis inhibitors. *Antimicrob. Agents Chemother.* **52**, 1703–1712 (2008).
9. Polikanov, Y. S. et al. Distinct tRNA accommodation intermediates observed on the ribosome with the antibiotics hygromycin A and A201A. *Mol. Cell* **58**, 832–844 (2015).
10. Toh, S. M., Xiong, L., Bae, T. & Mankin, A. S. The methyltransferase YfgB/RlmN is responsible for modification of adenosine 2503 in 23S rRNA. *RNA* **14**, 98–106 (2008).
11. Yan, F. et al. RlmN and Cfr are radical SAM enzymes involved in methylation of ribosomal RNA. *J. Am. Chem. Soc.* **132**, 3953–3964 (2010).
12. Grove, T. L. et al. A radically different mechanism for S-adenosylmethionine-dependent methyltransferases. *Science* **332**, 604–607 (2011).
13. Vazquez-Laslop, N., Ramu, H., Klepacki, D., Kannan, K. & Mankin, A. S. The key function of a conserved and modified rRNA residue in the ribosomal response to the nascent peptide. *EMBO J.* **29**, 3108–3117 (2010).
14. Ramu, H. et al. Nascent peptide in the ribosome exit tunnel affects functional properties of the A-site of the peptidyl transferase center. *Mol. Cell* **41**, 321–330 (2011).
15. Benitez-Paez, A., Villarroya, M. & Armengod, M. E. The *Escherichia coli* RlmN methyltransferase is a dual-specificity enzyme that modifies both rRNA and tRNA and controls translational accuracy. *RNA* **18**, 1783–1795 (2012).
16. Atkinson, G. C. et al. Distinction between the Cfr methyltransferase conferring antibiotic resistance and the housekeeping RlmN methyltransferase. *Antimicrob. Agents Chemother.* **57**, 4019–4026 (2013).
17. Madhaiyan, M., Wirth, J. S. & Saravanan, V. S. Phylogenomic analyses of the *Staphylococcaceae* family suggest the reclassification of five species within the genus *Staphylococcus* as heterotypic synonyms, the promotion of five subspecies to novel species, the taxonomic reassignment of five *Staphylococcus* species to *Mammaliicoccus* gen. nov., and the formal assignment of *Nosocomiicoccus* to the family *Staphylococcaceae*. *Int. J. Syst. Evol. Microbiol.* **70**, 5926–5936 (2020).
18. Schwarz, S., Werckenthin, C. & Kehrenberg, C. Identification of a plasmid-borne chloramphenicol-florfenicol resistance gene in *Staphylococcus sciuri*. *Antimicrob. Agents Chemother.* **44**, 2530–2533 (2000).
19. Toh, S. M. et al. Acquisition of a natural resistance gene renders a clinical strain of methicillin-resistant *Staphylococcus aureus* resistant to the synthetic antibiotic linezolid. *Mol. Microbiol.* **64**, 1506–1514 (2007).
20. Hansen, L. H., Planellas, M. H., Long, K. S. & Vester, B. The order Bacillales hosts functional homologs of the worrisome cfr antibiotic resistance gene. *Antimicrob. Agents Chemother.* **56**, 3563–3567 (2012).
21. Tsai, K. et al. Directed evolution of the rRNA methylating enzyme Cfr reveals molecular basis of antibiotic resistance. *eLife* **11**, e70017 (2022).
22. Schmeing, T. M., Huang, K. S., Strobel, S. A. & Steitz, T. A. An induced-fit mechanism to promote peptide bond formation and exclude hydrolysis of peptidyl-tRNA. *Nature* **438**, 520–524 (2005).
23. Polikanov, Y. S., Steitz, T. A. & Innis, C. A. A proton wire to couple aminoacyl-tRNA accommodation and peptide-bond formation on the ribosome. *Nat. Struct. Mol. Biol.* **21**, 787–793 (2014).
24. Svetlov, M. S. et al. Structure of Erm-modified 70S ribosome reveals the mechanism of macrolide resistance. *Nat. Chem. Biol.* **17**, 412–420 (2021).
25. Syroegin, E. A., Aleksandrova, E. V. & Polikanov, Y. S. Structural basis for the inability of chloramphenicol to inhibit peptide bond formation in the presence of A-site glycine. *Nucleic Acids Res.* **50**, 7669–7679 (2022).

26. Syroegin, E. A., Aleksandrova, E. V. & Polikanov, Y. S. Insights into the ribosome function from the structures of non-arrested ribosome-nascent chain complexes. *Nat. Chem.* **15**, 143–153 (2023).
27. Polikanov, Y. S., Melnikov, S. V., Soll, D. & Steitz, T. A. Structural insights into the role of rRNA modifications in protein synthesis and ribosome assembly. *Nat. Struct. Mol. Biol.* **22**, 342–344 (2015).
28. Tsai, K. et al. Structural basis for context-specific inhibition of translation by oxazolidinone antibiotics. *Nat. Struct. Mol. Biol.* **29**, 162–171 (2022).
29. Syroegin, E. A. et al. Structural basis for the context-specific action of the classic peptidyl transferase inhibitor chloramphenicol. *Nat. Struct. Mol. Biol.* **29**, 152–161 (2022).
30. Svetlov, M. S. et al. High-resolution crystal structures of ribosome-bound chloramphenicol and erythromycin provide the ultimate basis for their competition. *RNA* **25**, 600–606 (2019).
31. Tereshchenkov, A. G. et al. Binding and action of amino acid analogs of chloramphenicol upon the bacterial ribosome. *J. Mol. Biol.* **430**, 842–852 (2018).
32. Chen, C. W. et al. Binding and action of triphenylphosphonium analog of chloramphenicol upon the bacterial ribosome. *Antibiotics* **10**, 390 (2021).
33. Asai, T., Zaporojets, D., Squires, C. & Squires, C. L. An *Escherichia coli* strain with all chromosomal rRNA operons inactivated: complete exchange of rRNA genes between bacteria. *Proc. Natl Acad. Sci. USA* **96**, 1971–1976 (1999).
34. Hansen, J. L. et al. The structures of four macrolide antibiotics bound to the large ribosomal subunit. *Mol. Cell* **10**, 117–128 (2002).
35. Wu, K. J. Y., Klepacki, D., Mankin, A. S. & Myers, A. G. A method for tritiation of iboxamycin permits measurement of its ribosomal binding. *Bioorg. Med. Chem. Lett.* **91**, 129364 (2023).
36. Mitcheltree, M. J. et al. A synthetic antibiotic class overcoming bacterial multidrug resistance. *Nature* **599**, 507–512 (2021).
37. Brodiazhenko, T. et al. Synthetic oxepanoprolinamide iboxamycin is active against *Listeria monocytogenes* despite the intrinsic resistance mediated by VgaL/Lmo0919 ABCF ATPase. *JAC Antimicrob. Resist.* **4**, dlac061 (2022).
38. Obana, N. et al. Genome-encoded ABCF factors implicated in intrinsic antibiotic resistance in Gram-positive bacteria: VmlR2, Ard1 and CplR. *Nucleic Acids Res.* **51**, 4536–4554 (2023).
39. Pfister, P. et al. The structural basis of macrolide-ribosome binding assessed using mutagenesis of 23S rRNA positions 2058 and 2059. *J. Mol. Biol.* **342**, 1569–1581 (2004).
40. Liu, M. & Douthwaite, S. Resistance to the macrolide antibiotic tylosin is conferred by single methylations at 23S rRNA nucleotides G748 and A2058 acting in synergy. *Proc. Natl Acad. Sci. USA* **99**, 14658–14663 (2002).
41. Li, Q. et al. Synthetic group A streptogramin antibiotics that overcome Vat resistance. *Nature* **586**, 145–150 (2020).
42. Goethe, O., DiBello, M. & Herzon, S. B. Total synthesis of structurally diverse pleuromutilin antibiotics. *Nat. Chem.* **14**, 1270–1277 (2022).
43. Osterman, I. A. et al. Madumycin II inhibits peptide bond formation by forcing the peptidyl transferase center into an inactive state. *Nucleic Acids Res.* **45**, 7507–7514 (2017).
44. Dunkle, J. A., Xiong, L., Mankin, A. S. & Cate, J. H. Structures of the *Escherichia coli* ribosome with antibiotics bound near the peptidyl transferase center explain spectra of drug action. *Proc. Natl Acad. Sci. USA* **107**, 17152–17157 (2010).

Methods

Reagents

Unless stated otherwise, all chemicals and reagents were obtained from MilliporeSigma. IBX was synthesized following the protocols described previously[45]. All synthetic oligonucleotides, such as DNA primers and mRNA for structural studies, were obtained from Integrated DNA Technologies.

Phylogenetic analysis of *cfr* genes

To identify a large set of Cfr homologs from which proteins encoded by thermophiles could be selected, a BlastP search against the NCBI (https://www.ncbi.nlm.nih.gov/) Refseq database was carried out, with the CfrA from the Comprehensive Antibiotic Resistance Database (CARD)[46] as the query. An E-value cut-off of 1×10^{-70} was used, which allowed all available Cfr sequences to be identified, along with a subset of RlmN family homologs. The sequences were aligned using MAFFT-L-INS-I v.6.861b (ref. 47). After removing alignment positions with more than 50% gaps with TrimAl v.1.2 (ref. 48), preliminary phylogenetic analysis was carried out with FastTree v.2.1 (ref. 49) to distinguish Cfr representatives from the more distantly related RlmN, and to identify thermophilic Cfr representatives. For the representative tree shown in Supplementary Fig. 1, additional Cfr and RlmN representatives downloaded respectively from the CARD[46] and Uniprot[50] databases were aligned as above with the thermophile Cfr and other Cfr sequences of interest to this study. After a TrimAl step as above, phylogenetic analysis was carried out with IQTree v.2.1.2 (ref. 51) on the CIPRES Science Gateway[52] with 1,000 rapid bootstrap replicates and automatic model determination. All alignments and phylogenies are available from https://github.com/GCA-VH-lab/2023_Cfr.

Construction of the *cfr*$^+$ *T. thermophilus* HB27 strain

The original *cfr* gene from mesophilic *S. aureus* (*Sau*) encoding for A2503-C8-methylase as well as several homologous *cfr*-like genes from various moderately thermophilic bacterial species (Supplementary Table 1) were commercially synthesized de novo (the synthesis was carried out by GenScript) and cloned into the pBGAA1-BthERM expression vector, which we generated in our previous study[24]. The DNA sequences of the synthesized genes were adjusted to the codon usage for optimal gene expression in the *T. thermophilus* (*Tth*) HB27 host. The synthesized *cfr*-like genes were inserted in place of the *erm* gene, using *Nsi*I and *Ssp*I unique restriction sites, and placed under the control of the inducible P_{arg} promoter (Fig. 1b, orange). This vector originates from the parent pBGAA1 plasmid[53], which was specifically designed to replicate in *Tth* due to the presence of repA gene and oriV2 replication origin (Fig. 1b). It also carries the *hph* gene[54] which provides a high level of resistance to hygromycin B (HygB) at a broad range of temperatures from 37 °C to 65 °C and allows for positive selection (Fig. 1b, blue). The resulting expression vectors (Fig. 1b) were transformed into the *Tth* HB27 host, and cells were then propagated in standard liquid ATCC 697 medium supplemented with Castenholz salt. Transformants were plated on 3% agar plates prepared with the same medium. The agar plates were incubated at 60 °C for 24–48 h to allow colony formation. To select the *cfr*$^+$ colonies, transformed *Tth* cells were plated on agar containing 50 μg ml^{-1} HygB. Individual HygB-resistant colonies were picked, diluted in a fresh medium containing 50 μg ml^{-1} HygB and grown at 58 °C.

Construction of *rlmN*$^-$ *T. thermophilus* HB27 strain

Upstream and downstream homology regions (UHR and DHR, respectively) flanking the *Tth rlmN* coding sequence were amplified using the following primer pairs:

- 5′-TAAAACGACGGCCAGTGCCACCTCGAGGCCCTTCGCCC-3′ (UHR-Fwd);
- 5′-GTCCTTTCATACCCTCCCATTGTAGCCGAGAAG-3′ (UHR-Rev);
- 5′-ACCATTTTGATGACCCTCACACCGCTTCCAGAAG-3′ (DHR-Fwd);
- 5′-AGTCGACCTGCAGGCATGCACGCCTCGGACACGGCGCA-3′ (DHR-Rev).

The *htk* gene encoding a thermostable kanamycin adenyltransferase[55] was amplified using primer pair:

- 5′-ATGGGAGGGTATGAAAGGACCAATAATAATGAC-3′ (HTK-Fwd);
- 5′-GTGAGGGTCATCAAAATGGTATGCGTTTTG-3′ (HTK-Rev).

The obtained UHR, *htk* and DHR sequences were inserted into *HindIII*-digested plasmid pUC18 using the NEBuilder HiFi DNA Assembly Master Mix (E2621, New England Biolabs) following the manufacturer's protocol. The resulting assembly was used to transform NEB 5-alpha competent *E. coli* cells (C2987, New England Biolabs), and transformants were selected on LB ampicillin plates. *Tth* strain HB27 was transformed with the resulting plasmid, and recombinants were selected on TEM kanamycin plates. Individual *Tth* isolates were purified, sequenced to confirm the replacement of *rlmN* gene with *htk* gene and also analyzed by diagnostic PCR using primer pair no. 1:

- 5′-ATTCGACATATGGCCGCTTCCCACGCCCTC-3′;
- 5′-TTTTTCATATGATACCTCCTGTCATCGCCCGGCGCC-3′;

and primer pair no. 2:

- 5′-ATGAAAGGACCAATAATAATGACTAGAGAAGAAAGAATG-3′;
- 5′-TCAAAATGGTATGCGTTTTGACACATCCACTATATATCC-3′.

MIC determination assays

Initial antibiotic susceptibility testing of *T. thermophilus* cells transformed with expression vectors encoding various Cfr-like methylases was performed by a batch method using 1 ml of media (Supplementary Table 2). The values of MICs for different antibiotics against *T. thermophilus* HB27 (Supplementary Table 5) or *E. coli* SQ171 *ΔtolC* strains (Supplementary Table 4) were determined by liquid broth microdilution assay in sterile 96-well plates using a total volume of 100 μl per well. *T. thermophilus* HB27 strains carrying various pBGAA1 expression vectors were grown in ATCC 697-rich medium supplemented with Castenholz salt and containing 50 μg ml^{-1} HygB (selection marker). To minimize the negative effects of high temperature on the structure and activity of Cfr-like methylases, the MIC testing experiments were performed at 60 °C. *E. coli* SQ171 *ΔtolC* strains carrying plasmid-encoded WT or A2062G/U/C-mutant versions of the 23S rRNA gene[56–59] were grown in LB medium containing 100 μg ml^{-1} ampicillin. Exponentially growing cells were diluted to optical density $(OD)_{600}$ = 0.002 and incubated for 48 h at 60 °C (*T. thermophilus*) or overnight at 37 °C (*E. coli*) with 2-fold increasing concentrations of tested antibiotics. Cell viability was analyzed by staining with AlamarBlue dye (Bio-Rad). All MIC values were determined in triplicates and reported as their modal values.

Isolation and purification of A2503-C2,C8-dimethylated 70S ribosomes

The *Tth* HB27 cells expressing Cfr-like methylase from *P. fulgidum* were grown at 58–60 °C in flasks with a total of 9 l of ATCC 697 medium supplemented with Castenholz salt, 50 μg ml^{-1} HygB (to retain the Cfr expression vector) and 50 μg ml^{-1} CLI (to sustain high levels of induction of PfuCFR expression). The *cfr*$^+$ *Tth* cells were collected at early-to-mid log-phase (OD_{600} = 0.9–1.0) and used for the subsequent large-scale preparation of A2503-C2,C8-dimethylated 70S ribosomes. The total yield was approximately 19 g of cell paste. Purification of Cfr-methylated ribosomes was accomplished as optimized previously for the A2058-N6-dimethylated[24,36] as well as the WT[23,27] 70S ribosomes from *T. thermophilus*. We routinely use this procedure for the preparation of ribosomes for our crystallographic studies. The main steps of ribosome purification included cell lysis, sucrose cushion

ultracentrifugation, reverse-phase chromatography and, finally, separation of the tightly coupled 70S ribosomes from individual subunits by sucrose gradient centrifugation. The final 70S pellets were suspended in a buffer, flash-frozen in liquid nitrogen and stored at −80 °C until used in crystallization experiments.

Primer extension analysis

We used the property of reverse transcriptase to produce truncated cDNA products by stalling at the C2,C8-dimethylated adenine nucleotides to assess the extent of A2503-C8-methylation in the obtained *T. thermophilus* HB27 cells expressing PfuCFR. To this end, 23S rRNA isolated from the *cfr*$^+$, WT or *rlmN*$^-$ cells was analyzed by primer extension with SuperScript III Reverse Transcriptase (Invitrogen) according to the manufacturer's protocol. First, 2 pmol of radioactively 5′-[^{32}P]-labeled primer (5′-GCCCGTGGCGGATAGAGACCG-3′ or 5′- TCTTCAGCCCCAGGATGCGACGAGCCG-3′) was annealed with 1.25 µg of each of the three 23S rRNA samples. The primer extension reactions by reverse transcriptase were carried out at 50 °C in the presence of 0.5 mM of each dNTP (Figs. 1c) or 1 mM dATP, dCTP and dTTP, and 0.2 mM ddGTP (Fig. 1d). For the reactions with ddGTP, the extension time was decreased to 5 min, and the concentration of reverse transcriptase was reduced fourfold relative to that suggested in the manufacturer's protocol. Primer extension cDNA products were purified by phenol extraction, precipitated with ethanol and resolved on 6% polyacrylamide sequencing gels in TBE buffer. Gels were transferred onto Whatman paper, dried, exposed to the phosphorimager screen overnight and visualized in a Typhoon RGB phosphorimager (Cytiva).

X-ray crystallographic structure determination

To obtain high-resolution structures that would allow visualizing of structural features crucial for this study, we employed a strategy that relies on the use of hydrolysis-resistant aminoacylated tRNAs, which exhibit higher (than deacylated tRNAs) affinity to the 70S ribosome and better stabilize it in the unrotated state, resulting in noticeably higher resolution of the resulting datasets. Moreover, such complexes represent the functional pre-attack states of the ribosome. Synthetic mRNA with the sequence 5′-GGC-AAG-GAG-GUA-AAA-**AUG**-**UUC**-UAA-3′, containing the Shine–Dalgarno sequence followed by the P-site methionine and the A-site phenylalanine codons, was obtained from Integrated DNA Technologies. Nonhydrolyzable aminoacylated tRNAs, Phe-NH-tRNA^{Phe} and fMet-NH-tRNA$_i^{Met}$ were prepared as described previously[23,60]. Stable amide-linked peptidyl-tRNA (fMTHSMRC-tRNA$_i^{Met}$) was prepared as described previously[26].

Complexes of the A2503-C2,C8-dimethylated *T. thermophilus* 70S ribosomes with mRNA and hydrolysis-resistant A-site aminoacyl- (Phe-tRNA^{Phe}) and P-site aminoacyl- (fMet-tRNA$_i^{Met}$) or peptidyl- (fMTHSMRC-tRNA$_i^{Met}$) tRNAs were formed as described previously for deacylated[27] or aminoacylated tRNAs[23,24]. For *Tth* 70S ribosome complexes with IBX or TYL, both co-crystallization and soaking experimental approaches yielded identical results. We used 50 µM IBX and 500 µM TYL for structural studies.

Collection and processing of the X-ray diffraction data, model building and structure refinement were performed as described in our previous reports[23–27,36]. Diffraction data were collected using NE-CAT Remote Access software (v.6.2.3) at beamlines 24ID-C and 24ID-E at the Advanced Photon Source (Argonne National Laboratory). A complete dataset for each complex was collected using 0.979-Å irradiation at 100 K from multiple regions of the same crystal, using 0.3-degree oscillations. Raw data were integrated and scaled using XDS software (version 10 January 2022)[61]. Molecular replacement was performed using PHASER from the CCP4 program suite (v.7.0)[62]. The search model was generated from the previously published structures of *T. thermophilus* 70S ribosome with bound mRNA and aminoacylated tRNAs (PDB entries 6XHW (ref. 24) and 8CVL (ref. 26)). Initial molecular replacement solutions were refined by rigid-body refinement with the ribosome split into multiple domains, followed by positional and individual B-factor refinement using PHENIX Refine software (v.1.17)[63]. Noncrystallographic symmetry restraints were applied to four parts of the 30S ribosomal subunit (head, body, spur and helix 44) and four parts of the 50S subunit (body, L1-stalk, L10-stalk and C terminus of the L9 protein). Structural models were built in Coot (v.0.8.2)[64]. Structural models and restraints for IBX and TYL were generated using PHENIX eLBOW software (v.1.17)[63]. The statistics of data collection and refinement are compiled in Supplementary Table 3. All figures showing atomic models were generated using PyMol software (v.1.8; www.pymol.org).

Reporting summary

Further information on research design is available in the Nature Portfolio Reporting Summary linked to this article.

Data availability

Coordinates and structure factors were deposited in the RCSB Protein Data Bank with accession codes: 8G29 for the A2503-C2, C8-dimethylated *T. thermophilus* 70S ribosome in complex with mRNA, aminoacylated A-site Phe-NH-tRNA^{Phe}, aminoacylated P-site fMet-NH-tRNA$_i^{Met}$ and deacylated E-site tRNA^{Phe}; 8G2A for the A2503-C2,C8-dimethylated *T. thermophilus* 70S ribosome in complex with mRNA, aminoacylated A-site Phe-NH-tRNA^{Phe}, peptidyl P-site fMTHSMRC-NH-tRNA$_i^{Met}$ and deacylated E-site tRNA^{Phe}. 8G2B for the A2503-C2,C8-dimethylated *T. thermophilus* 70S ribosome in complex with mRNA, deacylated A-site tRNA^{Phe}, aminoacylated P-site fMet-NH-tRNA$_i^{Met}$, deacylated E-site tRNA^{Phe} and iboxamycin; 8G2C for the A2503-C2,C8-dimethylated *T. thermophilus* 70S ribosome in complex with mRNA, aminoacylated A-site Phe-NH-tRNA^{Phe}, aminoacylated P-site fMet-NH-tRNA$_i^{Met}$, deacylated E-site tRNA^{Phe} and tylosin; 8G2D for the wild-type *T. thermophilus* 70S ribosome in complex with mRNA, deacylated A-site tRNA^{Phe}, deacylated P-site tRNA$_i^{Met}$, deacylated E-site tRNA^{Phe} and tylosin. All previously published structures that were used in this work for structural comparisons were retrieved from the RCSB Protein Data Bank: PDB entries 6XHW, 8CVL, 7LVK, 7RQE, 7S1G, 7S1I, 5DOY, 5VP2, 4V7V, 7RQ8, 1K9M, 1KD1, 1K8A. No sequence data were generated in this study. Analyzed protein sequences are presented with their corresponding accession numbers in the phylogenetic tree (Supplementary Fig. 1) for retrieval from the NCBI protein database. Source data are provided with this paper.

References

45. Mason, J. D., Terwilliger, D. W., Pote, A. R. & Myers, A. G. Practical gram-scale synthesis of iboxamycin, a potent antibiotic candidate. *J. Am. Chem. Soc.* **143**, 11019–11025 (2021).
46. McArthur, A. G. et al. The Comprehensive Antibiotic Resistance Database. *Antimicrob. Agents Chemother.* **57**, 3348–3357 (2013).
47. Katoh, K. & Standley, D. M. MAFFT multiple sequence alignment software version 7: improvements in performance and usability. *Mol. Biol. Evol.* **30**, 772–780 (2013).
48. Capella-Gutierrez, S., Silla-Martinez, J. M. & Gabaldon, T. trimAl: a tool for automated alignment trimming in large-scale phylogenetic analyses. *Bioinformatics* **25**, 1972–1973 (2009).
49. Price, M. N., Dehal, P. S. & Arkin, A. P. FastTree 2—approximately maximum-likelihood trees for large alignments. *PLoS ONE* **5**, e9490 (2010).
50. UniProt, C. Uniprot The universal protein knowledgebase in 2023. *Nucleic Acids Res.* **51**, D523–D531 (2023).
51. Nguyen, L. T., Schmidt, H. A., von Haeseler, A. & Minh, B. Q. IQ-TREE: a fast and effective stochastic algorithm for estimating maximum-likelihood phylogenies. *Mol. Biol. Evol.* **32**, 268–274 (2015).
52. Miller, M. A. et al. A RESTful API for access to phylogenetic tools via the CIPRES science gateway. *Evol. Bioinform. Online* **11**, 43–48 (2015).

53. Carr, J. F., Danziger, M. E., Huang, A. L., Dahlberg, A. E. & Gregory, S. T. Engineering the genome of *Thermus thermophilus* using a counterselectable marker. *J. Bacteriol.* **197**, 1135–1144 (2015).
54. Nakamura, A., Takakura, Y., Kobayashi, H. & Hoshino, T. In vivo directed evolution for thermostabilization of *Escherichia coli* hygromycin B phosphotransferase and the use of the gene as a selection marker in the host-vector system of *Thermus thermophilus*. *J. Biosci. Bioeng.* **100**, 158–163 (2005).
55. Hashimoto, Y., Yano, T., Kuramitsu, S. & Kagamiyama, H. Disruption of *Thermus thermophilus* genes by homologous recombination using a thermostable kanamycin-resistant marker. *FEBS Lett.* **506**, 231–234 (2001).
56. Douthwaite, S., Powers, T., Lee, J. Y. & Noller, H. F. Defining the structural requirements for a helix in 23S ribosomal RNA that confers erythromycin resistance. *J. Mol. Biol.* **209**, 655–665 (1989).
57. Bollenbach, T., Quan, S., Chait, R. & Kishony, R. Nonoptimal microbial response to antibiotics underlies suppressive drug interactions. *Cell* **139**, 707–718 (2009).
58. Kannan, K., Vazquez-Laslop, N. & Mankin, A. S. Selective protein synthesis by ribosomes with a drug-obstructed exit tunnel. *Cell* **151**, 508–520 (2012).
59. Quan, S., Skovgaard, O., McLaughlin, R. E., Buurman, E. T. & Squires, C. L. Markerless *Escherichia coli* rrn deletion strains for genetic determination of ribosomal binding sites. *G3* **5**, 2555–2557 (2015).
60. Gamper, H. & Hou, Y.M. tRNA 3′-amino-tailing for stable amino acid attachment. *RNA* **24**, 1878–1885 (2018).
61. Kabsch, W. XDS. *Acta Crystallogr. D* **66**, 125–132 (2010).
62. McCoy, A. J. et al. PHASER crystallographic software. *J. Appl. Crystallogr.* **40**, 658–674 (2007).
63. Adams, P. D. et al. PHENIX: a comprehensive Python-based system for macromolecular structure solution. *Acta Crystallogr. D* **66**, 213–221 (2010).
64. Emsley, P. & Cowtan, K. Coot: model-building tools for molecular graphics. *Acta Crystallogr. D* **60**, 2126–2132 (2004).

Acknowledgements

We thank A. Mankin and N. Vazquez-Laslop for providing *E. coli* SQ171 Δ*tolC* strains and for valuable discussions. We thank the staff at NE-CAT beamlines 24ID-C and 24ID-E for help with X-ray diffraction data collection, especially M. Capel, F. Murphy, S. Banerjee, I. Kourinov, D. Neau, J. Schuermann, N. Sukumar, A. Lynch, J. Withrow, K. Perry, A. Kaya and C. Salbego. This work is based upon research conducted at the Northeastern Collaborative Access Team beamlines, which are funded by the National Institute of General Medical Sciences from the National Institutes of Health (NIH) (grant on. P30-GM124165 to NE-CAT). The Eiger 16M detector on 24ID-E beamline is funded by an NIH-ORIP HEI grant (grant no. S10-OD021527 to NE-CAT). This research used resources of the Advanced Photon Source, a US Department of Energy (DOE) Office of Science User Facility operated for the DOE Office of Science by Argonne National Laboratory under contract no. DE-AC02-06CH11357. This work was supported by the National Institute of Allergy and Infectious Diseases of the NIH (grant no. R01-AI168228 to A.G.M. and grant no. R21-AI163466 to Y.S.P.), the National Institute of General Medical Sciences of the NIH (grant no. R01-GM094157 to S.T.G. and grant no. R01-GM132302 to Y.S.P.), the National Science Foundation (grant no. MCB-1907273 to Y.S.P.), the USDA National Institute for Food and Agriculture (Hatch Project no. 1016013 to S.T.G.), the Illinois State startup funds (to Y.S.P.), the Swedish Research Council (Ventenskapsrådet) (grant nos. 2019-01085 and 2022-01603 to G.C.A.), the Knut and Alice Wallenberg Foundation (grant no. 2020.0037 to G.C.A.) and the Carl Tryggers Stiftelse för Vetenskaplig Forskning (grant no. CTS19:24 to G.C.A.). K.J.Y.W. was supported by a National Science Scholarship (Ph.D.) from the Agency for Science, Technology and Research (Singapore). The funders had no role in study design, data collection and analysis, decision to publish or manuscript preparation.

Author contributions

E.V.A. with help from S.M.B. and M.S.S. constructed the *T. thermophilus* HB27 strain expressing Cfr-like methylases. G.C.A. performed phylogenetic analysis and identified putative thermostable *cfr*-like genes. B.I.C.T. and K.J.Y.W. synthesized iboxamycin. E.E.K. prepared Δ*rlmN* knock-out *T. thermophilus* HB27 strain. E.V.A. performed the assessment of A2503-C8-methylation using primer extension assay. E.V.A. and E.A.S. grew *T. thermophilus* cells and purified Cfr-modified 70S ribosomes. E.A.S. and E.V.A. prepared hydrolysis-resistant aminoacyl- and peptidyl-tRNAs. E.V.A. with help from B.I.C.T. and K.J.Y.W. performed microbiological assays. E.V.A., E.A.S. and Y.S.P. designed and performed X-ray crystallography experiments. A.G.M., Y.S.P. and S.T.G. supervised the experiments. All authors interpreted the results. E.V.A., B.I.C.T., K.J.Y.W., A.G.M. and Y.S.P. wrote the manuscript.

Competing interests

A.G.M. is an inventor in a provisional patent application submitted by the President and Fellows of Harvard College covering oxepanoprolinamide antibiotics described in this work. A.G.M. has filed the following international patent applications: WO/2019/032936 'Lincosamide Antibiotics and Uses Thereof' and WO/2019/032956 'Lincosamide Antibiotics and Uses Thereof'. The other authors declare no competing interests.

Additional information

Extended data is available for this paper at https://doi.org/10.1038/s41589-023-01525-w.

Supplementary information The online version contains supplementary material available at https://doi.org/10.1038/s41589-023-01525-w.

Correspondence and requests for materials should be addressed to Andrew G. Myers or Yury S. Polikanov.

Peer review information *Nature Chemical Biology* thanks the anonymous reviewers for their contribution to the peer review of this work.

https://doi.org/10.1038/s41589-023-01525-w

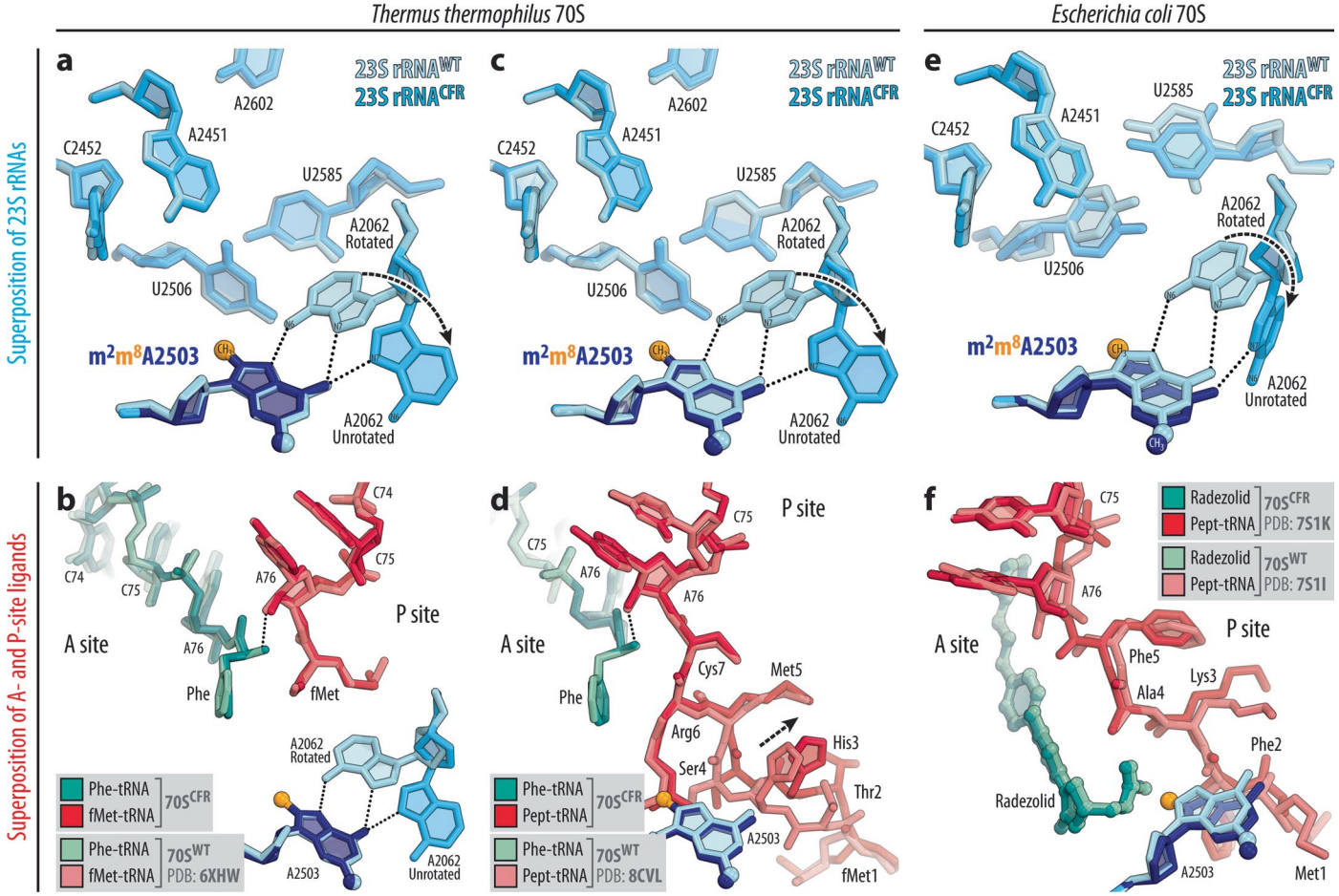

Extended Data Fig. 1 | Comparison of the structures of Cfr-modified and wild-type 70S ribosomes from *T. thermophilus* and *E. coli*. Superpositioning of the previously reported structures of *T. thermophilus* WT 70S ribosome containing aminoacylated Phe-tRNA^{Phe} in the A site and either fMet-tRNA$_i^{Met}$ (**a, b**; PDB entry 6XHW ref. 24) or fMTHSMRC-peptidyl tRNA$_i^{Met}$ (**c, d**; PDB entry 8CVL ref. 26) in the P site, or *E. coli* WT 70S ribosome containing radezolid in the A site and fMFKAF-peptidyl-tRNA^{Phe} in the P site (**e, f**; PDB entry 7S1I ref. 28) with the structures of the same complexes containing Cfr-modified nucleotide A2503 of the 23S rRNA. All structures were aligned based on domain V of the 23S rRNA. (**a, c, e**) Comparisons of the positions of key 23S rRNA nucleotides around the PTC. (**b, d, f**) Comparisons of the positions of A- and P-site substrates relative to nucleotides A2062 and A2503. Nucleotides of the Cfr-modified and unmodified ribosomes are shown in blue and light blue, espectively. The Cfr-modified residue A2503 is highlighted in navy blue, with the C8-methyl group shown in orange. *E. coli* nucleotide numbering is used. H-bonds are shown with dotted lines.

https://doi.org/10.1038/s41589-023-01525-w

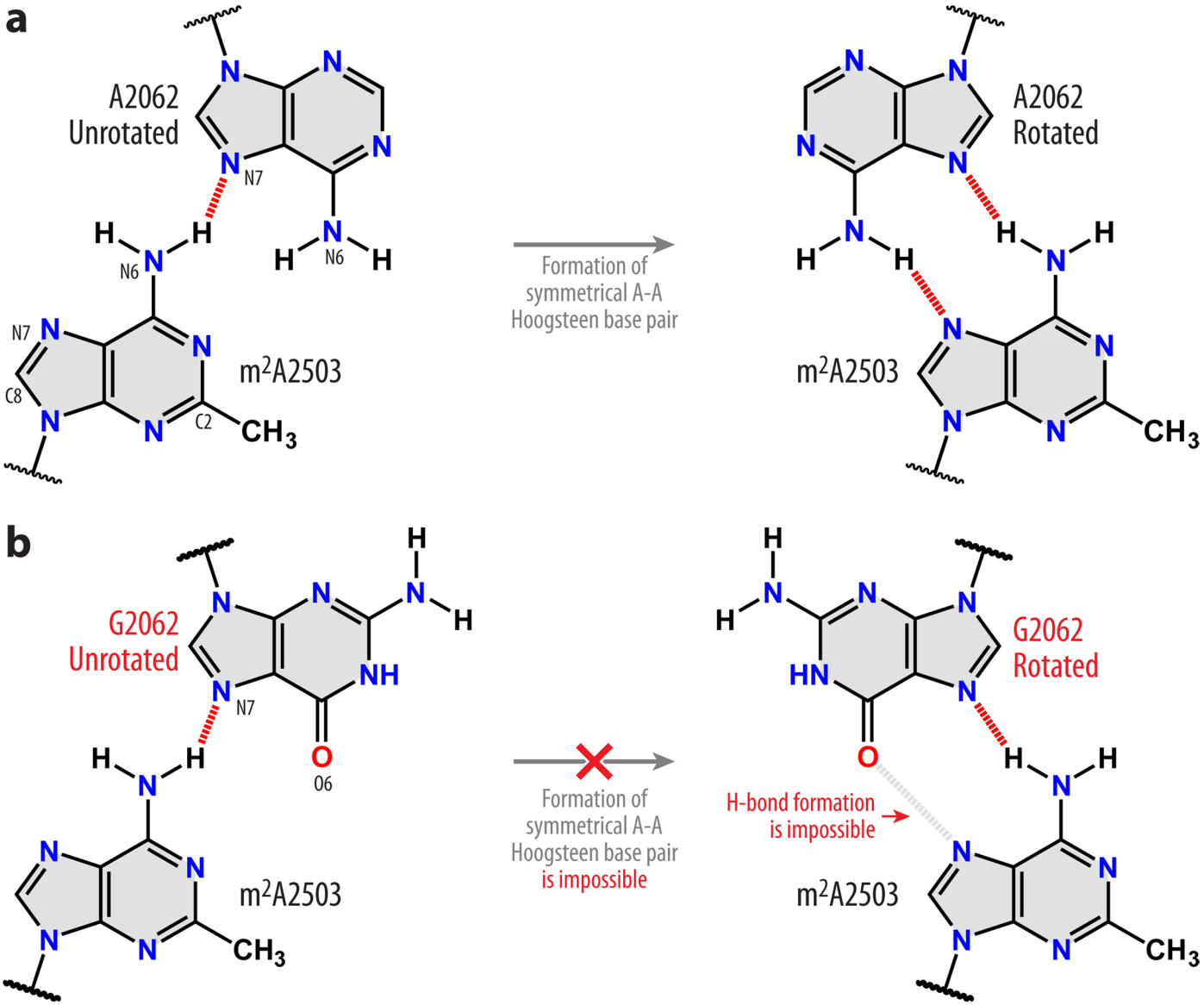

Extended Data Fig. 2 | Schematic diagrams of H-bond rearrangement between nucleotides in position 2062 and A2503 of the 23S rRNA upon Hoogsteen base pair formation. (**a**) Formation of the symmetric trans A-A Hoogsteen base pair between A2062 and m^2A2503 observed in the structures of 70S ribosome. Note that the formation of this base pair requires the N7-atoms of both adenines to be deprotonated in order to serve as H-bond acceptors of the N6-protons of the base-paired nucleotide. (**b**) The same Hoogsteen base pair is impossible with a guanine nucleotide in position 2062 of the 23S rRNA due to the inability to form an H-bond between O6 of G2062 and N7 of m^2A2503.

https://doi.org/10.1038/s41589-023-01525-w

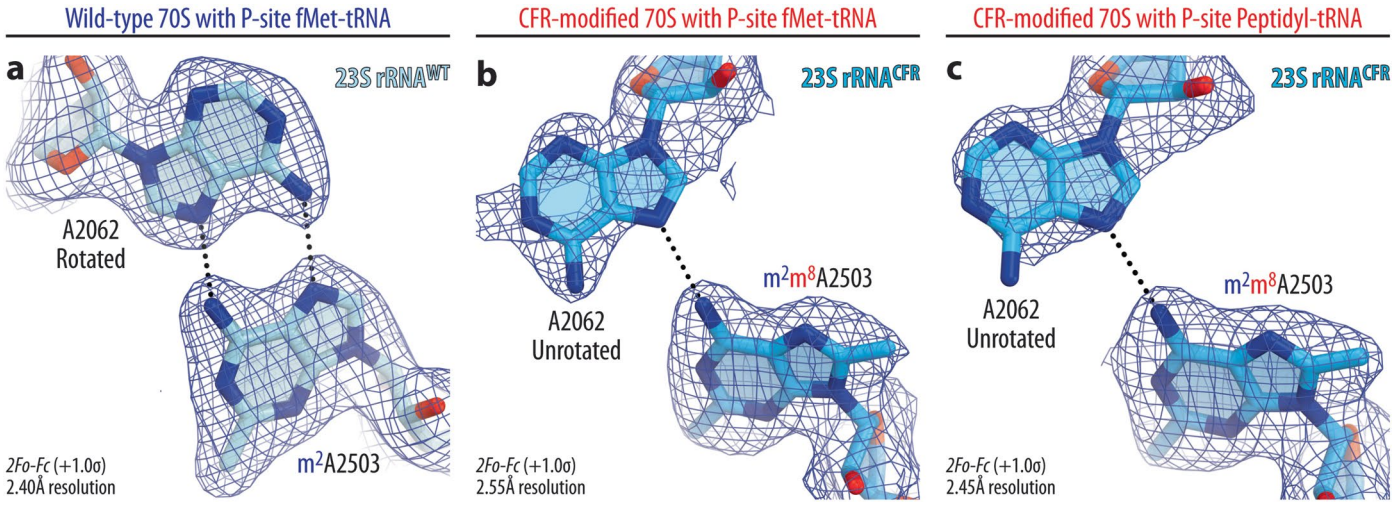

Extended Data Fig. 3 | Electron density maps of 23S rRNA in wild-type and Cfr-modified *T. thermophilus* 70S ribosome. $2F_o$-F_c electron difference Fourier maps (blue mesh) of A2062 and A2503 residues of 23S rRNA in the wild-type (**a**) or Cfr-modified (**b, c**) *T. thermophilus* 70S ribosome carrying aminoacylated Phe-tRNA^{Phe} in the A site and either fMet-tRNA$_i^{Met}$ (a, b) or fMTHSMRC-peptidyl-tRNA$_i^{Met}$ (c) in the P site. The structure and the electron density map of the wild-type ribosome complex (a) are from PDB entry 6XHW ref. 24. Carbon atoms are colored light blue for the C8-unmethylated A2503 (a) and blue for the Cfr-modified A2503 (b, c); nitrogens are dark blue; oxygens are red.

https://doi.org/10.1038/s41589-023-01525-w

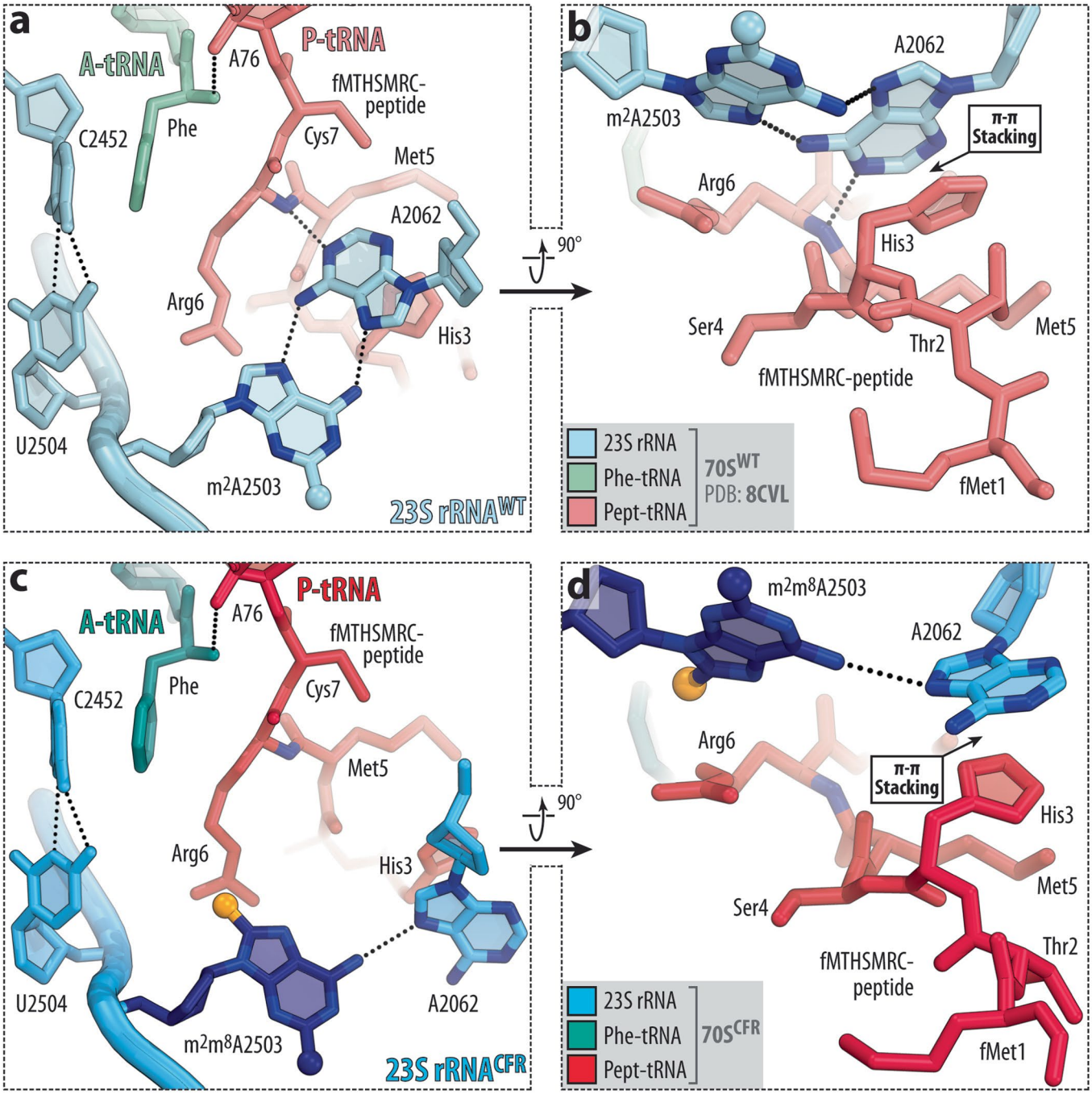

Extended Data Fig. 4 | Interactions of fMTHSMRC-peptidyl-tRNAs with wild-type and Cfr-modified *T. thermophilus* 70S ribosome. Close-up views of the aminoacyl and peptidyl moieties of A-site Phe-tRNA^{Phe} and P-site fMTHSMRC-tRNA$_i^{Met}$ in the wild-type (**a, b**; PDB entry 8CVL ref. 26) or Cfr-modified (**c, d**) *T. thermophilus* 70S ribosome. H-bonds are shown by black dotted lines. Stacking interactions between the aromatic side chain of His3 of fMTHSMRC-peptidyl-tRNA and A2062 nucleobase of the 23S rRNA are indicated by a black arrow.

https://doi.org/10.1038/s41589-023-01525-w

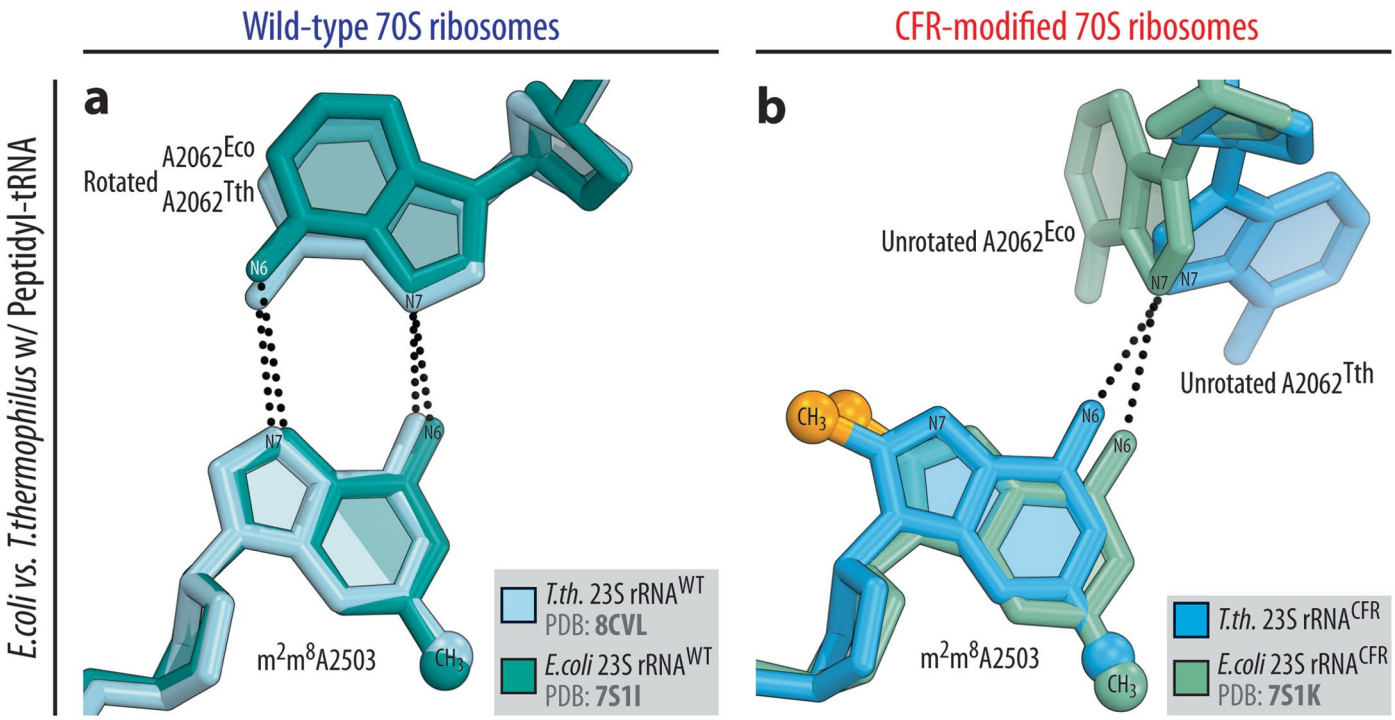

Extended Data Fig. 5 | Comparison of the structures of WT and Cfr-modified ribosomes from *E. coli* and *T. thermophilus*. (**a**) Superpositioning of the previous structures of WT 70S ribosomes carrying P-site peptidyl-tRNAs from *T. thermophilus* (light blue, PDB entry 8CVL ref. 26) and *E. coli* (teal, PDB entry 7S1I ref. 28). (**b**) Superpositioning of the new structure of Cfr-modified 70S ribosome carrying P-site peptidyl-tRNAs from *T. thermophilus* (blue) and *E. coli* (light teal, PDB entry 7S1K ref. 28).

https://doi.org/10.1038/s41589-023-01525-w

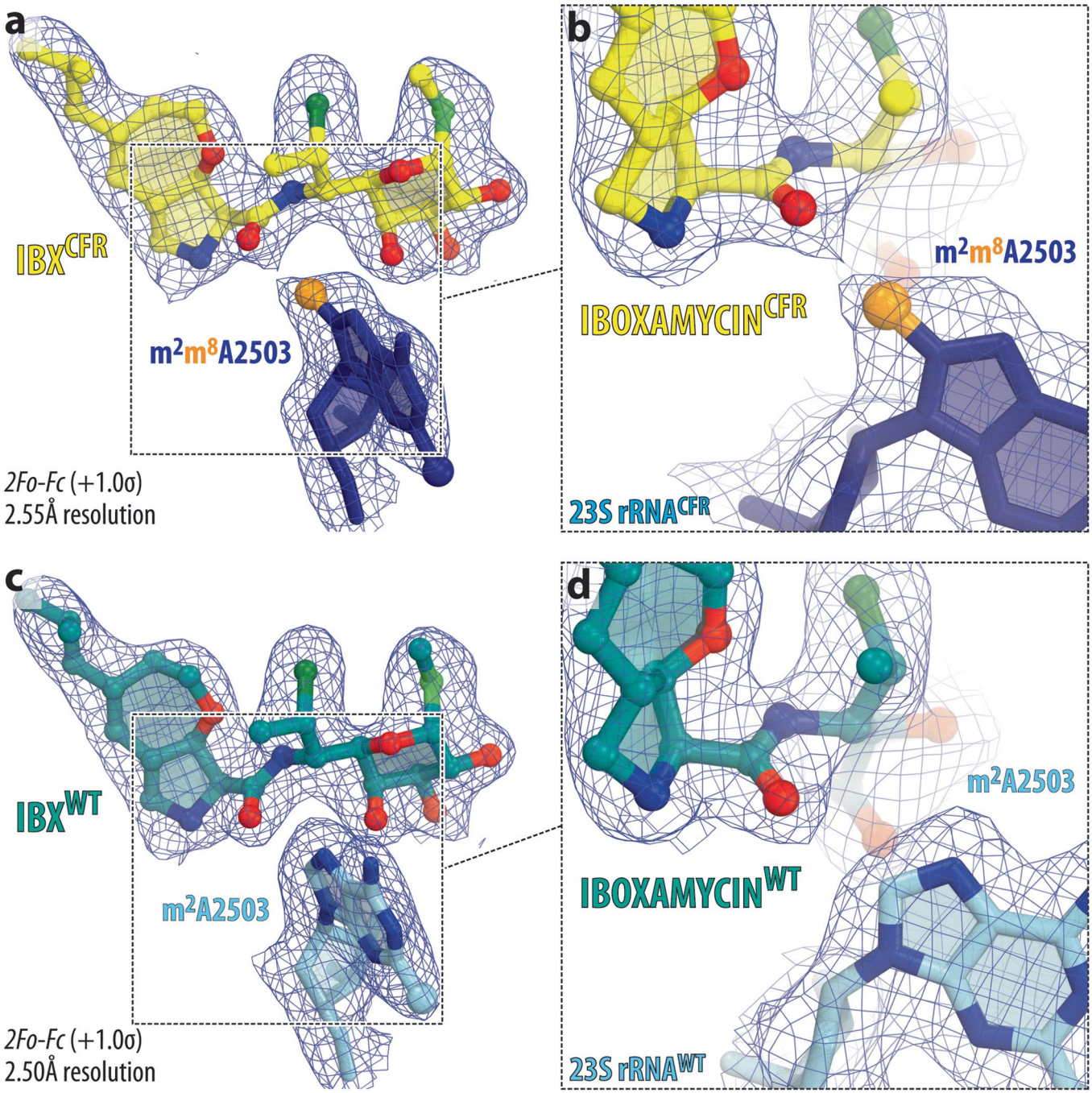

Extended Data Fig. 6 | Comparison of electron density maps of iboxamycin (IBX) in complex with Cfr-modified and wild-type *T. thermophilus* 70S ribosomes. $2F_o$-F_c electron density maps (blue mesh) contoured at 1.0σ of IBX in complex with Cfr-modified (**a, b**, yellow) or wild-type (**c, d**, teal) *T. thermophilus* 70S ribosomes. The C8-methyl group of m^2m^8A2503 is highlighted in orange. The structure and the electron density map of IBX in complex with wild-type 70S ribosome (c, d) are from PDB entry 7RQ8 ref. 36. Carbon atoms are colored navy blue for the Cfr-modified m^2m^8A2503 (a, b) and light blue for the WT m^2A2503 (c, d); nitrogens are dark blue; oxygens are red.

https://doi.org/10.1038/s41589-023-01525-w

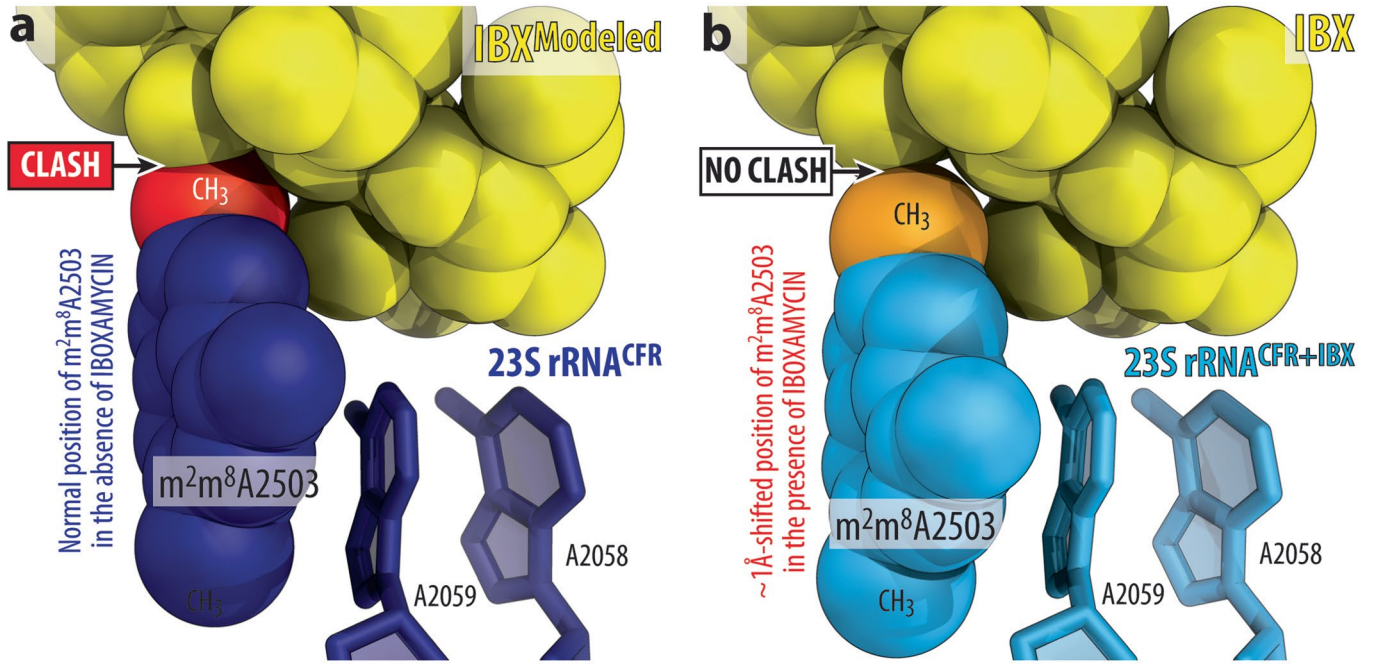

Extended Data Fig. 7 | Comparison of the m^2m^8A2503 positions in the Cfr-modified ribosome in the presence and absence of iboxamycin. (**a**) Superposition of the structures of drug-free Cfr-modified 70S ribosome containing m^2m^8A2503 residue (shown as navy blue spheres with C8-methyl group highlighted in red) with the structure of ribosome-bound iboxamycin (IBX, yellow). (**b**) Structure of Cfr-modified 70S ribosome containing m^2m^8A2503 residue (shown as blue spheres with C8-methyl highlighted in orange) in complex with iboxamycin (IBX, yellow). Note that binding of iboxamycin to the Cfr-modified ribosome causes an ~1 Å shift of the m^2m^8A2503 residue away from the drug.

https://doi.org/10.1038/s41589-023-01525-w

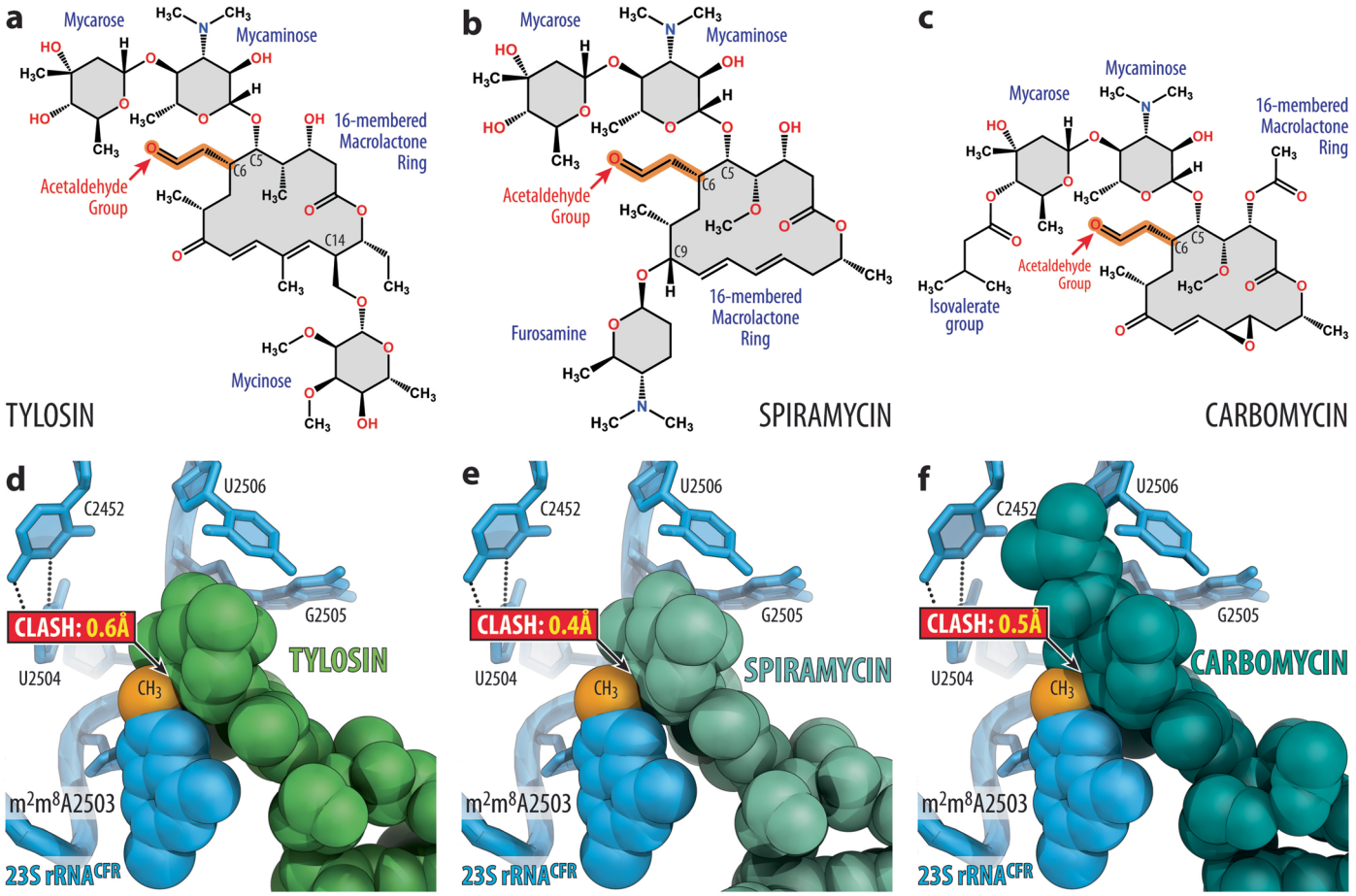

Extended Data Fig. 8 | Structural basis for the Cfr-mediated resistance to 16-membered macrolides. (**a**–**c**) Chemical structures of tylosin (a), spiramycin (b), and carbomycin (c). (**d-f**) Superposition of the structures of Cfr-modified *T. thermophilus* 70S ribosome containing C8-methylated A2503 residue in the 23S rRNA (blue) with the previously reported structures of 16-membered macrolides, such as tylosin (d, green; PDB entry 1K9M ref. 34), spiramycin (e, light teal; PDB entry 1KD1 ref. 34), or carbomycin (f, tealF PDB entry 1K8A ref. 34) in complex with the 50S ribosomal subunit from the archaeon *H. marismortui*. The degrees of steric overlaps between the C8-methyl group of the m^2m^8A2503 nucleotide and each PTC-acting drug are shown in yellow. These numbers reflect the distance in Å that the drug and the m^2m^8A2503 residue need to move away from each other to avoid the steric clash. Note that the C8-methyl group of m^2m^8A2503 (highlighted in orange) can physically interfere with the binding of 16-membered macrolides.

https://doi.org/10.1038/s41589-023-01525-w

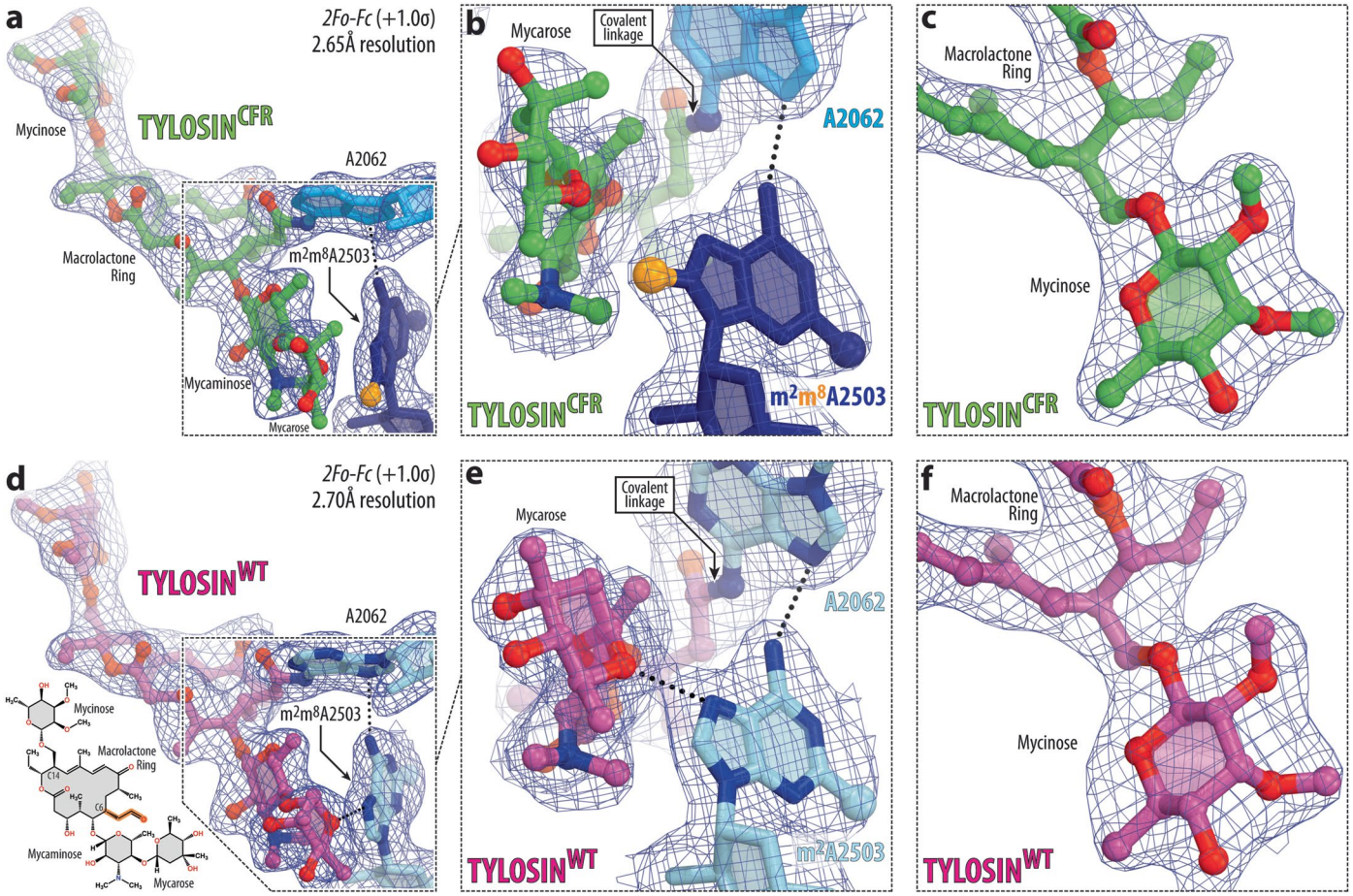

Extended Data Fig. 9 | Structures of tylosin (TYL) bound to the Cfr-modified and WT 70S ribosomes. (**a**–**f**) Electron density map (blue mesh) contoured at 1.0σ of TYL (green or magenta) in complex with the Cfr-modified (**a**–**c**) or wild-type (**d**–**f**) *T. thermophilus* 70S ribosome containing m^2m^8A2503 (dark blue with C8-methyl group highlighted in orange) or m^2A2503 (light blue) residues in the 23S rRNA, respectively. The chemical structure of tylosin is shown in panel d. The reactive acetaldehyde group (highlighted in red) at C6 of tylosin's macrolactone ring forms a covalent bond with the exocyclic N6-amino group of A2062 in the *T. thermophilus* ribosome. Note that the mycinose moiety at C14 of the macrolactone ring of tylosin is well-resolved in the electron density maps.

https://doi.org/10.1038/s41589-023-01525-w

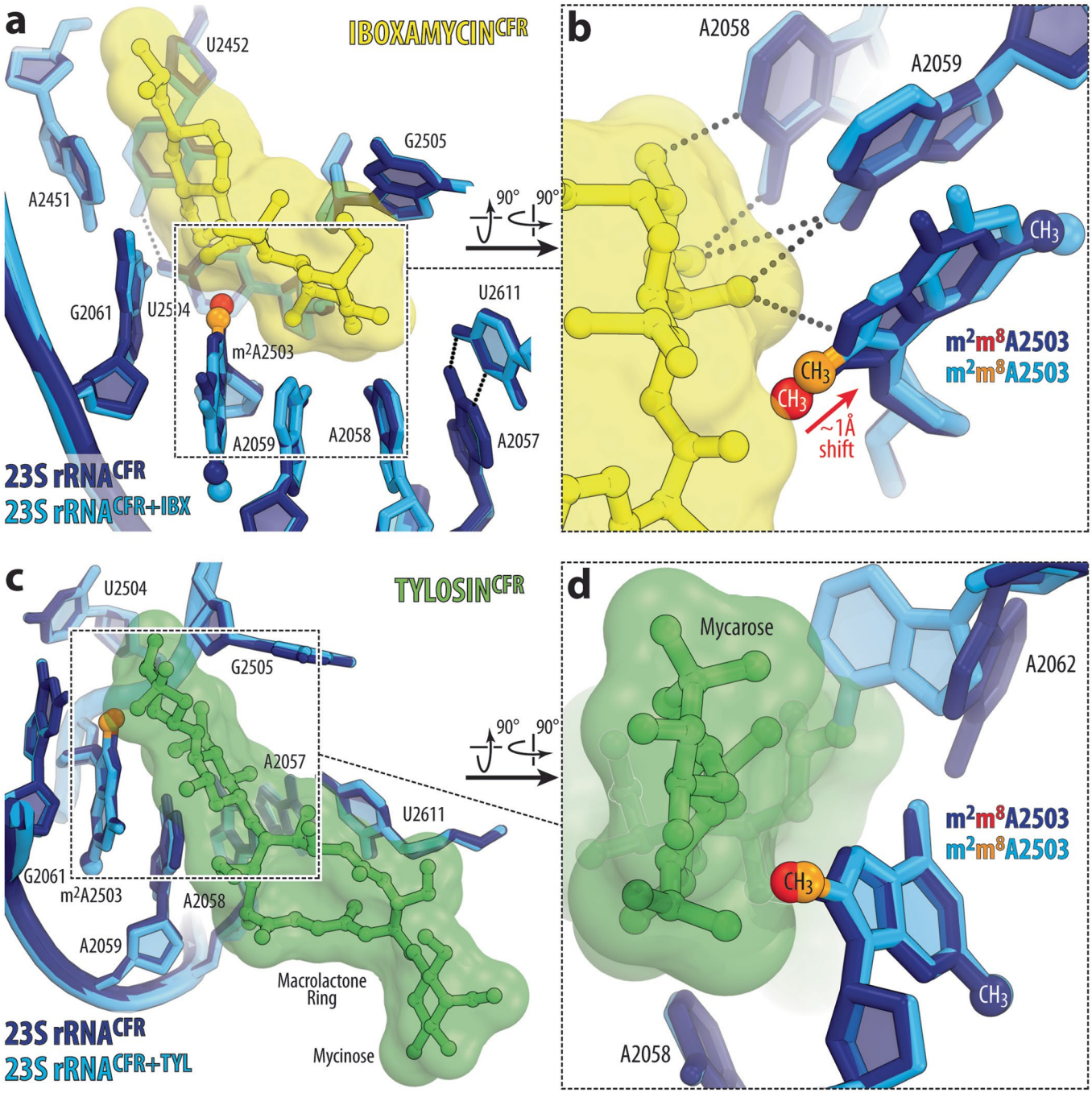

Extended Data Fig. 10 | Comparisons of A2503 positions in Cfr-modified ribosomes in the presence and absence of iboxamycin or tylosin. Superposition of the structures of Cfr-modified 70S ribosome both containing m^2m^8A2503 residue in the presence (blue) and absence (navy blue) of iboxamycin (**a, b**, yellow) or tylosin (**c, d**, green). Note that while binding of iboxamycin to the Cfr-modified ribosome causes an ~1 Å shift of m^2m^8A2503 residue away from the drug, binding of tylosin does not affect the position of the m^2m^8A2503 residue.

nature portfolio

Corresponding author(s): Andrew G. Myers & Yury S. Polikanov

Last updated by author(s): Nov 13, 2023

Reporting Summary

Nature Portfolio wishes to improve the reproducibility of the work that we publish. This form provides structure for consistency and transparency in reporting. For further information on Nature Portfolio policies, see our Editorial Policies and the Editorial Policy Checklist.

Statistics

For all statistical analyses, confirm that the following items are present in the figure legend, table legend, main text, or Methods section.

n/a	Confirmed
☐	☒ The exact sample size (*n*) for each experimental group/condition, given as a discrete number and unit of measurement
☒	☐ A statement on whether measurements were taken from distinct samples or whether the same sample was measured repeatedly
☒	☐ The statistical test(s) used AND whether they are one- or two-sided *Only common tests should be described solely by name; describe more complex techniques in the Methods section.*
☒	☐ A description of all covariates tested
☒	☐ A description of any assumptions or corrections, such as tests of normality and adjustment for multiple comparisons
☒	☐ A full description of the statistical parameters including central tendency (e.g. means) or other basic estimates (e.g. regression coefficient) AND variation (e.g. standard deviation) or associated estimates of uncertainty (e.g. confidence intervals)
☒	☐ For null hypothesis testing, the test statistic (e.g. *F*, *t*, *r*) with confidence intervals, effect sizes, degrees of freedom and *P* value noted *Give P values as exact values whenever suitable.*
☒	☐ For Bayesian analysis, information on the choice of priors and Markov chain Monte Carlo settings
☒	☐ For hierarchical and complex designs, identification of the appropriate level for tests and full reporting of outcomes
☒	☐ Estimates of effect sizes (e.g. Cohen's *d*, Pearson's *r*), indicating how they were calculated

Our web collection on statistics for biologists contains articles on many of the points above.

Software and code

Policy information about availability of computer code

Data collection	X-ray diffraction data was collected at beamlines 24ID-C and 24ID-E at the Advanced Photon Source (Argonne National Laboratory) using NE-CAT Remote Access software v6.2.3.
Data analysis	Raw X-ray diffraction crystallographic data were integrated and scaled using XDS software (version Jan 10, 2022). Molecular replacement was performed using PHASER from the CCP4 program suite (version 7.0). All structures were refined using PHENIX Refine software (version 1.17). Structural models were built in Coot (version 0.8.2). Structural models and restraints for IBX and TYL were generated using PHENIX eLBOW software (version 1.17). All figures showing atomic models were generated using PyMol software (version 1.8).

For manuscripts utilizing custom algorithms or software that are central to the research but not yet described in published literature, software must be made available to editors and reviewers. We strongly encourage code deposition in a community repository (e.g. GitHub). See the Nature Portfolio guidelines for submitting code & software for further information.

Data

Policy information about availability of data

All manuscripts must include a data availability statement. This statement should provide the following information, where applicable:

- Accession codes, unique identifiers, or web links for publicly available datasets
- A description of any restrictions on data availability
- For clinical datasets or third party data, please ensure that the statement adheres to our policy

Coordinates and structure factors were deposited in the RCSB Protein Data Bank with accession codes:
• 8G29 for the A2503-C2,C8-dimethylated T. thermophilus 70S ribosome in complex with mRNA, aminoacylated A-site Phe-NH-tRNAPhe, aminoacylated P-site fMet-NH-tRNAiMet, and deacylated E-site tRNAPhe;
• 8G2A for the A2503-C2,C8-dimethylated T. thermophilus 70S ribosome in complex with mRNA, aminoacylated A-site Phe-NH-tRNAPhe, peptidyl P-site fMTHSMRC-NH-tRNAiMet, and deacylated E-site tRNAPhe.
• 8G2B for the A2503-C2,C8-dimethylated T. thermophilus 70S ribosome in complex with mRNA, deacylated A-site tRNAPhe, aminoacylated P-site fMet-NH-tRNAiMet, deacylated E-site tRNAPhe, and iboxamycin;
• 8G2C for the A2503-C2,C8-dimethylated T. thermophilus 70S ribosome in complex with mRNA, aminoacylated A-site Phe-NH-tRNAPhe, aminoacylated P-site fMet-NH-tRNAiMet, deacylated E-site tRNAPhe, and tylosin;
• 8G2D for the wild-type T. thermophilus 70S ribosome in complex with mRNA, deacylated A-site tRNAPhe, deacylated P-site tRNAiMet, deacylated E-site tRNAPhe, and tylosin;

All previously published structures that were used in this work for structural comparisons were retrieved from the RCSB Protein Data Bank: PDB entries 6XHW, 8CVL, 7LVK, 7RQE, 7S1G, 7S1I, 5DOY, 5VP2, 4V7V, 7RQ8, 1K9M, 1KD1, 1K8A.

No sequence data were generated in this study. Analyzed protein sequences are presented with their corresponding accession numbers in the phylogenetic tree (Supplementary Fig. 1) for retrieval from the NCBI protein database.

Human research participants

Policy information about studies involving human research participants and Sex and Gender in Research.

Reporting on sex and gender	Not Applicable
Population characteristics	Not Applicable
Recruitment	Not Applicable
Ethics oversight	Not Applicable

Note that full information on the approval of the study protocol must also be provided in the manuscript.

Field-specific reporting

Please select the one below that is the best fit for your research. If you are not sure, read the appropriate sections before making your selection.

☒ Life sciences ☐ Behavioural & social sciences ☐ Ecological, evolutionary & environmental sciences

For a reference copy of the document with all sections, see nature.com/documents/nr-reporting-summary-flat.pdf

Life sciences study design

All studies must disclose on these points even when the disclosure is negative.

Sample size	No statistical methods were used to predetermine the sample size (number of repetitions) for the MIC experiments. Sample sizes of n=3 were a compromise between experimental cost and ability to generate reliable and statistically significant data.
Data exclusions	No data were excluded from the analyses.
Replication	MICs were determined in biological triplicates. The primer extension assays shown in Figure 1c and 1d each represent one of the three independent experiments. All attempts at replication were successful.
Randomization	Randomization in general is not relevant to this study. MIC determination assay was intrinsically randomized, as the experimental groups constituted equally sized aliquots of a common suspension of bacterial cells. For cross-validation during crystallographic model building and refinement, an R-free set was used. Other parts of model building and refinement did not require randomization because the outcomes of these experiments are not dependent on the judgment of the researcher and depend on the reference experiments that cannot be affected by unconscious bias.

Blinding	Blinding was not used in MIC assay because the outcome (turbidity) is not deemed subjective outside the margin of error (one binary dilution) typical for this experiment. Blinding was not used in the primer extension assays because the outcomes (differences in the positions of the primer extension termination sites) are evident upon inspection of the unprocessed gel images. Blinding was not used in X-ray crystallographic experiments, because the outcomes of these experiments are not dependent on the judgment of the researcher and depend on the reference experiments that cannot be affected by unconscious bias.

Reporting for specific materials, systems and methods

We require information from authors about some types of materials, experimental systems and methods used in many studies. Here, indicate whether each material, system or method listed is relevant to your study. If you are not sure if a list item applies to your research, read the appropriate section before selecting a response.

Materials & experimental systems

n/a	Involved in the study
☒	☐ Antibodies
☒	☐ Eukaryotic cell lines
☒	☐ Palaeontology and archaeology
☒	☐ Animals and other organisms
☒	☐ Clinical data
☒	☐ Dual use research of concern

Methods

n/a	Involved in the study
☒	☐ ChIP-seq
☒	☐ Flow cytometry
☒	☐ MRI-based neuroimaging